



rijksuniversiteit  
groningen

---

# Transient Grating Spectroscopy of Magnetic Thin Films

---

## THESIS

submitted in partial fulfillment of the  
requirements for the degree of

MASTER OF SCIENCE  
in  
APPLIED PHYSICS

Author : Timen Jansma  
Student ID : s1903705  
Supervisor : Dr. R.I. (Ra'anan) Tobey  
*2<sup>nd</sup>* corrector : Prof. Dr. T. (Tamalika) Banerjee

Groningen, The Netherlands, August 10, 2016



# Transient Grating Spectroscopy of Magnetic Thin Films

**Timen Jansma**

Zernike Institute for Advanced Materials, University of Groningen  
P.O. Box 221, NL-9700 AE, Groningen, The Netherlands

August 10, 2016

## Abstract

Materials that exhibit coupling between elastic and magnetic degrees of freedom are of both fundamental and technological interest. Such ‘magnetoelastic’ materials possess great potential for tuneable multifunctional devices and show opportunities for application in novel types of magnetic data storage, in which the generation of elastic waves lead to precessional switching of the magnetic orientation. In this report we use an all-optical approach to investigate the magnetoelastic properties of several ferromagnetic thin films. The ‘transient grating’ (TG) geometry is employed, in which the interference of two intense, spatially and temporally overlapped pump pulses are used to excite a ‘transient’ grating on the sample surface. This leads to the excitation of frequency tunable (surface) acoustic waves and, using a weaker probe pulse, the setup allows us to witness simultaneously both the acoustic waves and their coupling to the sample magnetization in real-time at sub-picosecond resolution. The sensitivity of the magnetization detection scheme in the TG setup is closely linked to temperature-induced partial demagnetization of the sample. The primary goal of this work is to understand the details of the temperature dynamics after optical excitation and how they affect the magnetization dynamics. In order to fully reconstruct the magnetization in time, it is therefore necessary to carefully consider the temperature dynamics inside the sample after excitation. Numerical simulations are performed to calculate the temperature dynamics with picosecond time resolution. The result of the simulations are used to correct the amplitudes of the magnetization precession of experimental data sets appropriately, revealing the ‘real’ magnetization dynamics as a function of time. As a secondary goal, we began a new experimental activity to study the magnetoelastic effects in the strongly magnetostriuctive material ‘Terfenol’. The results show multiple fundamental departures from previous measurements on nickel films. Whereas the response in nickel showed the resonant elastic driving of magnetization precession, in Terfenol, the most striking effect is the apparent complete, field-periodic, suppression of elastic wave propagation. Understanding of the remarkable results for Terfenol is still limited, and additional experimental work is needed as well as a clear theoretical framework. Nonetheless, these effects are remarkable in their ability to control thermal expansion and strain generation using magnetic fields.

---

v

---

v



# Contents

<b>1</b>	<b>Introduction</b>	<b>1</b>
<b>2</b>	<b>Experimental Setup</b>	<b>5</b>
2.1	The Pump-Probe Setup	5
2.2	The Transient Grating Setup	8
2.3	The Faraday Detection Scheme	12
2.4	Conclusion	14
<b>3</b>	<b>Theory</b>	<b>15</b>
3.1	Sample Excitation	15
3.1.1	Acoustic Waves and TG Diffraction Detection	15
3.1.2	Magnetoelastic Coupling and Faraday Rotation Detection	18
3.2	The Influence of Temperature on Magnetization Dynamics and its Detection	22
3.2.1	the Two-Temperature Model	22
3.2.2	Thermal Boundary Resistance	23
3.2.3	Temperature Dependence of Magnetization	24
3.3	Conclusion	26
<b>4</b>	<b>Temperature Dynamics and Magnetic Contrast of Thin Nickel Films in the Transient Grating setup</b>	<b>27</b>
4.1	Introduction	27
4.2	Application of the Two-Temperature Model	28
4.3	Numerical Simulation of Single Pump Temperature Dynamics - a 1D Model	29
4.3.1	Determination of Thermal Boundary Resistance for Nickel/SLG and Nickel/MgO Interfaces	31

4.4	Numerical Simulation of Transient Grating Temperature Dynamics - a 2D Model	33
4.4.1	Sample Dimensions and Meshing	33
4.4.2	Initial Temperature Distribution	34
4.4.3	Physics Applied to the Model	36
4.5	Determination of Magnetization Dynamics and Magnetooptic Sensitivity	36
4.6	Results: Temperature, Magnetization and Contrast Dynamics	38
4.6.1	Discussion of an Exemplary Result	38
4.6.2	Influence of Fluence, Film Thickness, Grating Wavelength, and Substrate Material on Magnetooptic Sensitivity	43
4.6.3	Correction of Experimental Fluence Dependences	50
4.7	Conclusion and Outlook	52
<b>5</b>	<b>Magnetoelastic Dynamics in Strongly Magnetostrictive Terfenol</b>	<b>53</b>
5.1	Introduction	53
5.2	Results	53
5.2.1	Faraday Rotation	54
5.2.2	Transmission TG Diffraction	56
5.3	Conclusion and Outlook	60
<b>6</b>	<b>Conclusion</b>	<b>61</b>

# Introduction

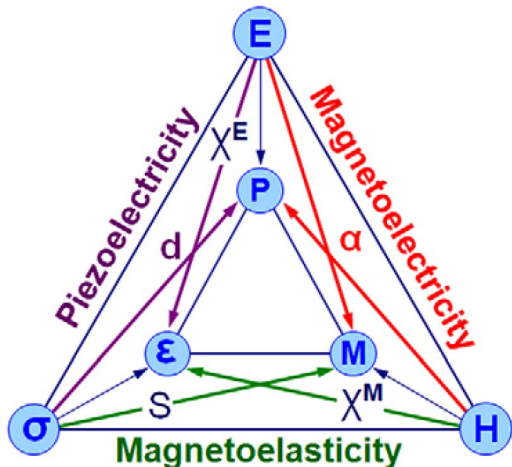


**Figure 1.1:** Schematic illustrating the three ferroic order parameters - ferroelectricity (E), ferromagnetism (H) and ferroelasticity ( $\sigma$ ) - and their coupling via the polarizability (P), magnetization (M) and strain ( $\epsilon$ ). Adapted from [1].

The search for high-speed, low-energy data storage devices in the present age in which digital information is proliferating and increasing exponentially, has led to both solid state devices as well as magnetic solutions. In the search for fast and low-cost data writing and storage techniques, much attention has been directed towards the utilization of multiferroics. By definition, multiferroics are materials that show more than one of the three ferroic order parameters simultaneously - ferroelectricity, ferromagnetism and ferroelasticity. After receiving some initial attention in the 60s and 70s in which magnetoelectric materials (materials in which coupling

occurs between the ferromagnetic and ferroelectric order parameter) were studied [2], technological advances and better theoretical understanding have stimulated an increasing number of research activities on multiferroics since the early 2000s [3]. Improved techniques for producing high-quality crystalline samples and thin films, along with advances in theoretical and computational methods, have led to the identification and understanding of new types of multiferroics [3–5], opening the door to many novel types of device applications. Most research is focused on magnetoelectrics, with the researcher’s incentive being the prospect of finding a material in which charge can be manipulated using magnetic fields or in which spins can be controlled with electric fields.

Precessional magnetization switching has proven to be a suitable candidate for future data writing methods [6, 7]. This precessional switching can be accomplished by two orthogonal magnetic field pulses along the soft and hard axes [7]. A different route is to use elastic wave pulses [8]. With this method, the challenge is to tune the elastic pulse strength, duration and frequency in such a way that the magnetization starts precessing and subsequently relaxes into the opposite orientation in a predictable fashion. The phenomenon of magnetization precession due to elastic deformations is a type of ‘magnetoelastic’ coupling, *i.e.* coupling between elastic and magnetic degrees of freedom. The foundation of magnetoelectrics has been well-established for several decades [9, 10]. There are two main routes for generating these elastic waves: 1) excitation through all-electric interdigitated transducers (IDTs) [11–13] and 2) ultrafast all-optical excitation [14–16]. The IDTs consist of interdigitated metal electrodes that launch narrowband radio-frequency surface acoustic waves (SAWs) of up to several GHz in a piezoelectric substrate on which the magnetic film is mounted. Optical methods are not limited by such complex sample structures, but lead in most cases to broadband longitudinal acoustic waves. They can generate strain amplitudes larger by several orders of magnitude than transducer-based methods, enabling studies in the nonlinear regimes.

In this study we investigate magnetoelastic coupling in ferromagnetic materials using all-optical methods of excitation. We employ various optical methods to launch narrow-band acoustic waves in our samples. To do this we use the so-called ‘transient grating’ technique [17] - an optical technique belonging to the class of pump-probe experiments, which creates a spatially periodic excitation pattern on a sample. This generates various acoustic modes, including frequency tunable surface acoustic waves. Using ultrashort laser pulses, this setup allows us to transiently follow both the elastic and magnetic dynamics simultaneously with sub-

picosecond resolution. The samples under our investigation are ferromagnetic thin films, ranging from polycrystalline nickel to more exotic materials such as single-crystal epitaxial Terfenol, which are mounted onto transparent, nonmagnetic substrate materials such as glass, MgO and sapphire.

The motivation of our experiments is to gain understanding of the stresses and magnetic states inside the studied materials and how they relate to each other. Coupling between these two degrees of freedom is observed in several of these materials, providing possibilities for applications and further research in the fields of, for example, optical spin pumping and low-power magnetization switching [8].

The transient grating setup poses additional challenges during the detection of magnetic dynamics. The spatially non-uniform excitation profile and the resulting alignment of spins makes the experimental sensitivity to the (local) magnetization of the sample nontrivial. A careful analysis and simulation of temperature dynamics inside the magnetic film is performed alongside the experimental work in order to obtain accurate and representative results for the magnetic behavior.



Chapter **2**

# Experimental Setup

For the work presented in this thesis, three primary experimental schemes need to be considered. In the first instance, standard pump-probe spectroscopy is required to accurately measure sample temperature evolution. Secondly, the majority of the work relies on a special case of pump-probe spectroscopy called ‘transient grating’ (TG) spectroscopy, where a spatially inhomogeneous excitation of the sample surface generates narrow-band surface propagating acoustic waves. Finally, in our special implementation of TG, we incorporate also magneto-optical measurements to assess the average magnetization of the sample. Each technique is discussed separately below.

## 2.1 The Pump-Probe Setup

Our approach to studying magnetoelastic phenomena is based on ultra-fast optical techniques, where we monitor, in real time, the dynamics of the sample after it is perturbed out of equilibrium by a pulse of light. The manner in which this so-called pump-probe technique is implemented provides access to a range of dynamical processes such as electronic, magnetic and structural dynamics.

In the conventional pump-probe experiment (Figure 2.1), short pulses of light called the pump and probe beams are focused and spatially overlapped on the sample surface. The more intense pump pulse triggers dynamics in the sample material, and a time-delayed probe pulse subsequently measures the change in optical properties. The time delay can be tuned to probe dynamics from the femtosecond to nanosecond scale and beyond. By carefully selecting the pump and probe photon energies,

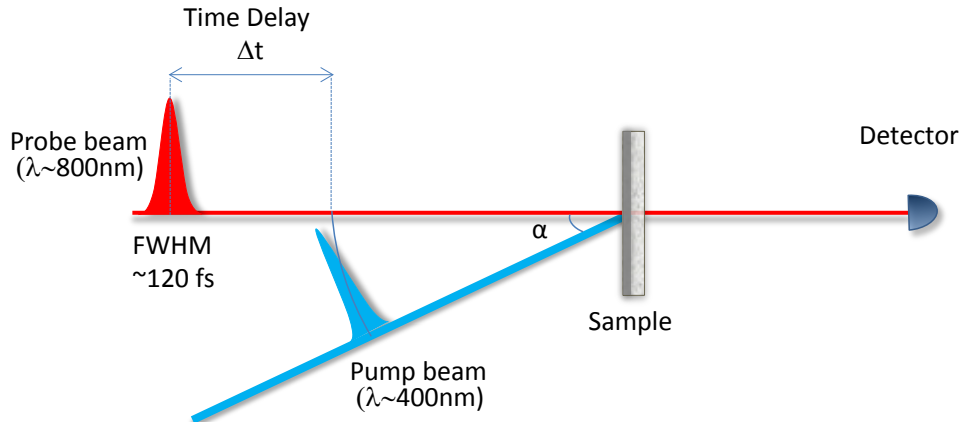


**Figure 2.1:** Pump-probe setup. One pump beam and one probe beam are spatially overlapped onto the sample surface with variable time delay. The transmitted probe beam carries information of the optical properties of the sample and goes to a photodetector.

as well as a careful consideration of the experimental geometry, specific information can be extracted about individual degrees of freedom in the material. Common examples of pump-probe techniques include ultrafast magneto optics measurements to understand magnetization dynamics, or ultrafast x-ray and electron techniques to study structural dynamics. In this thesis, we combine two specialty spectroscopies to generate and detect acoustic waves in materials while simultaneously measuring the average magnetization response via magneto optical methods.

For the particular experiments discussed in this thesis, we implement a two-color (nondegenerate) pump-probe scheme, where the pump photon energy is frequency shifted to 3 eV (400 nm), while the probe is kept at the laser fundamental of 1.5 eV (800 nm). The more intense pump pulse causes ultrafast excitation of the sample, triggering electronic excitation, which, over time, are distributed to a range of internal degrees of freedom such as magnetic orientation and lattice vibrations. The lower intensity probe pulse subsequently monitors the resulting dynamics of the various material properties of the sample. The dynamical response caused by the pump is measured by capturing the transmitted probe beam with a photodetector, where the transmission of the (800 nm) probe can be enhanced or diminished due to the dynamics of the material parameters following excitation. In this way, the materials dynamics are encoded onto the probe beam parameters such as intensity or polarization. The output of the

pump probe experiment is a time trace, which shows the encoded material dynamics as a function of time delay between excitation and probing. For our samples and timescales, the pump-probe setup is mostly sensitive to temperature dynamics (see Section 4.2).

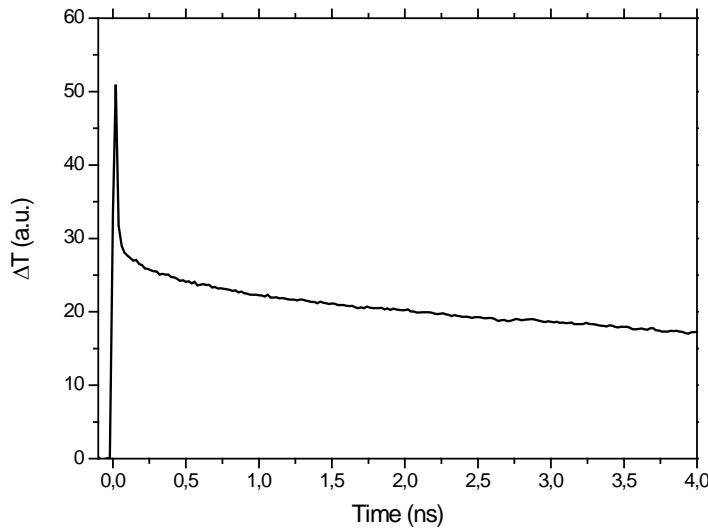


**Figure 2.2:** Sample pump-probe trace. Excitation by the pump pulse occurs at time  $t = 0$ . Subsequent changes in the sample transmission  $T$  are a measure of the sample temperature.

A representative pump-probe time trace is shown in Figure 2.2. Initially, before  $t = 0$ , no pump-induced change in probe intensity is measured by the detector. At  $t = 0$ , the pump and probe pulses are simultaneously incident on the sample, which is clearly visible by the large spike in probe intensity. After this initial excitation, the probe intensity is modified (reducing in the figure) as the sample cools and returns to its ground state.

For the purposes of this thesis, pump-probe measurements as depicted in Figure 2.1 are used to accurately determine the temperature dynamics of the film/substrate heterostructure. As will be discussed in Chapter 3, to understand the temperature evolution at the interface between two dissimilar materials, one must understand the ‘thermal boundary resistance’ present due to the differences in phonon density of states for the two materials. This quantity is of importance in performing accurate simulations of the temperature dynamics in the transient grating geometry, which is the main topic of Section 4.4. The theory of the thermal boundary resistance is included in Chapter 3. In Chapter 4 the quantity is determined

for nickel/SLG and nickel/MgO samples.

The experiments discussed in this thesis utilizes a turn-key ultrafast laser system called the ‘Legend Elite’ produced by Coherent Inc. In this system, pulses from a mode-locked Ti:Sapph oscillator are amplified, resulting in  $\approx 120 \text{ fs}$  pulses of wavelength  $\lambda = 800 \text{ nm}$ ,  $E = 5 \text{ mJ}$  at a  $1 \text{ kHz}$  repetition rate. Attenuated pulses are polarized and directed to the experiment, where each pulse is split into pump and probe pulses using appropriate optics. The pump beam is sent to a delay stage, providing up to  $8 \text{ ns}$  of time delay between the pump and probe pulse by adjusting the pump path length. The pump pulses are frequency-doubled to  $\lambda = 400 \text{ nm}$  using a BBO crystal.

The samples that we measure consist of thin magnetic films such as nickel on transparent substrates, such as soda lime glass (SLG, microscope slide), sapphire or MgO. Nickel films are prepared using Electron Beam Physical Vapor Deposition (EBPVD) in the clean room. Additional layers are added in some cases, such as protective capping layers.

## 2.2 The Transient Grating Setup

The main focus of this thesis is the study of magnetic materials in the transient grating (TG) geometry. TG is an extended version of the pump-probe setup discussed in the previous section, and as such, has many commonalities. It involves, however, a more complex method of excitation leading to additional dynamics.

The transient grating setup uses two, spatially-interfering, pump pulses leading to a spatially inhomogeneous excitation of the sample surface. The general TG setup is shown in Figure 2.3, where two  $400 \text{ nm}$  pulses are shown to overlap at the sample surface. In our experimental implementation, the crossing of the two pump pulses is ensured by imaging a diffractive phase mask onto the sample (for example, in the figure the imaging condition is provided by a two-lens imaging system). The phase masks that we use (produced by Toppan Photomasks) are optimized for maximum first order diffraction efficiency at the pump wavelength  $\lambda = 400 \text{ nm}$ , thus providing for the largest possible pump intensity. The excitation wavelength  $\Lambda$  is calculable using standard diffraction and imaging formulas, ultimately resulting in wavelengths as small as  $2 \mu\text{m}$  at the sample position. The pattern generated on the sample surface is an optical image of the phase mask, but since only the first-order diffracted beams are used to form the image, the result is a sinusoidal modulation instead of the square wave pattern of the phase mask. As an extension of pump-

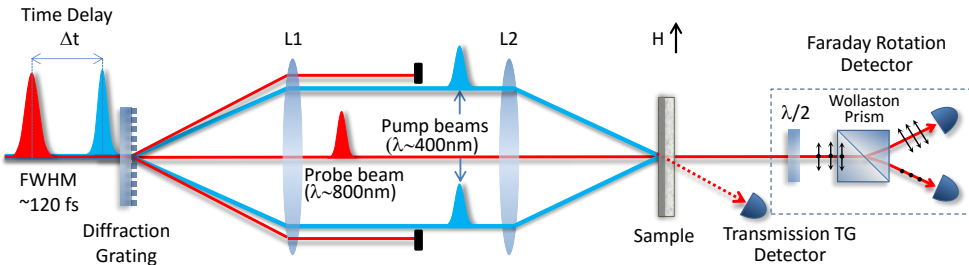


**Figure 2.3:** Transient grating (TG) setup. Two pump beams and one probe beam are spatially overlapped onto the sample surface with variable time delay. The pump beams create a spatially periodic interference pattern (see Figure 4.10), diffracting the probe pulse into several pulses traveling in different directions. The zero-order diffracted pulse (direct transmission) is polarization-analyzed in a Faraday detection scheme. The first-order diffracted probe pulse is captured by a single photodetector. An additional degree of freedom is introduced by placing the sample in a magnetic field  $H$  of variable strength parallel to the grating wavevector  $\mathbf{k}$ .

probe methodologies, the periodic excitation profile in the TG configuration leads to additional dynamics. The modulation in intensity heats the sample inhomogeneously, introducing lateral carrier and heat diffusion. Furthermore, the wave-like excitation profile leads to spatially periodic expansion of the sample, launching acoustic wave modes along the surface (see Section 3.1).

The probing of the spatially inhomogeneous dynamics can be performed in a number of ways. In our experimental setup, the 800 nm probe pulse also traverses a nearly identical optical path, while the choice of probing geometry also provides a means of selecting which dynamics are accessed. The mask has a low diffraction efficiency for the probe wavelength, and as a result, the zero-order diffracted probe pulse has sufficient energy and is used to follow the various material properties. The difference with the simple pump-probe geometry is that in the TG setup, the pump-induced spatial wavelike excitation profile modulates the sample properties (such as density) and acts as a ‘transient’ diffraction grating for the probe pulse. As the probe is incident on the sample after it has been excited, it is split into a central transmitted probe pulse and two first-order diffraction pulses. This also occurs in reflection, but this is not employed in this study. Each beam of the probe provides different information of the sample dynamics.

The undiffracted probe beam is sensitive to the average material prop-

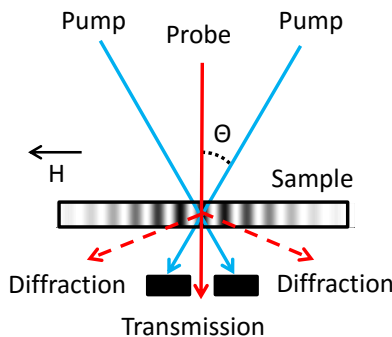


**Figure 2.4:** A spatially periodic pattern is created by interference of the two overlapped pump pulses. This results in splitting and diffracting of the probe pulse. The zero- and first-order diffracted probe pulses are captured and carry different types of information about the sample properties.

erties, which, for the case here, are largely determined by the sample temperature. Although the temperature profile is not uniform in the TG configuration, the central probe is sensitive to the average value, and time traces are therefore similar to the case of single-pump excitation (see Figure 2.2).

Detection of the diffracted probe pulse is the signature of the TG setup. Its intensity can be transiently followed by placing a detector - named the ‘transmission TG detector’ in Figure 2.3 - at a specific angle  $\theta$  behind the sample. The correct angle for placing the detector is determined by calculating the first-order diffraction angle using the grating wavelength  $\Lambda$  and the probe wavelength of 800 nm:

$$\theta = \arcsin\left(\frac{\lambda_{probe}}{\Lambda}\right), \quad (2.1)$$

Figure 2.5a shows an example transmission TG time trace for a nickel film on an SLG substrate, averaged over multiple loops. The pump-induced grating on the sample has wavelength  $\Lambda = 1.97 \pm 0.02 \mu m$ . The shape of the curve is quite similar to the pump probe trace (Figure 2.2), but shows additional oscillatory behavior, a characteristic not observed using the simple pump-probe technique. The oscillations are due to acoustic waves that are being launched by the transient grating. The TG technique can be used to study elastic characteristics of many types of materials. As an example, Figure 2.5b shows curves of some initial experimental work on the silicone polydimethylsiloxaan (PDMS). Three traces are presented: the blue curve shows a transmission TG time trace for nickel under the

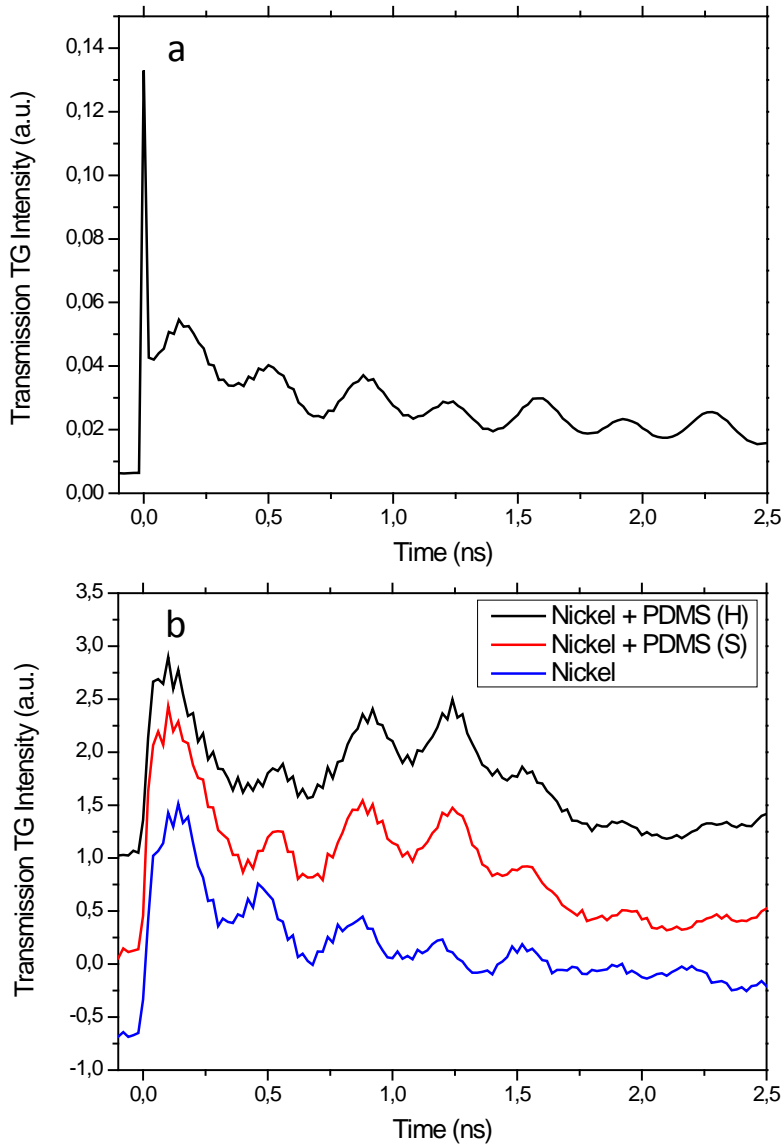


**Figure 2.5:** Sample time traces of transmission TG detection. The curves shows oscillations due to the presence of acoustic waves, which is not observed using basic pump-probe traces. (a) Time trace of a nickel film on an SLG substrate, averaged over multiple loops. (b) Addition of a 'hard' (H) and 'soft' (S) transparent PDMS layer on the nickel layer. In all cases, nickel film thickness  $d = 40 \text{ nm}$ , grating wavelength  $\Lambda = 1.97 \pm 0.02 \mu\text{m}$

same conditions as for the trace in Figure 2.5a. The black and red curve shows TG curves for nickel samples on which a layer of the transparent PDMS has been applied, where black contains elastically ‘hard’ PDMS and red ‘soft’ PDMS. It can be seen that the samples with added PDMS show rather similar behavior as the bare nickel sample. They are however not identical. The samples with PDMS (both hard and soft) show an additional lower frequency oscillation superposed on top of the bare nickel sample. Such clear differences between data from samples with and without added PDMS layer provides information about the elastic properties of PDMS.

It can be noticed that panel (b) has lower signal-to-noise levels than panel (a). This is mostly due to the fact that the traces in panel (b) are single loops rather than averages. Furthermore, for these ‘overlayer’ experiments, where we place a soft polymer onto the nickel films, the sample is excited ‘through the back,’ meaning that the substrate side faces the incoming pump and probe beams. This may affect the signal to noise ratio. Probing through the substrate was also found to diminish the initial ‘spike’ at  $t = 0$ .

### 2.3 The Faraday Detection Scheme

To augment the transient grating geometry, we implement a new capability that measures the magnetization dynamics simultaneously to the elastic dynamics. The simultaneous measurement of magneto-optical properties, implemented in the Faraday geometry, provides details of the average magnetization dynamics of the sample under study. Magneto-optical measurements encode the sample magnetization direction and amplitude onto the polarization state of the probe beam and thus a careful measurement of the latter as a function of time provides for the temporal evolution of the material magnetization.

Magneto-optics schemes are well-known in both static and dynamic measurement of material properties, and measuring the polarization of light is now a common experimental technique. The Faraday detection scheme is schematically depicted in Figure 2.3. Due to the sample magnetization (and dynamics), the probe undergoes small changes in polarization angle and ellipticity passing through the sample, typically less than 1 degree. An optical bridge geometry is utilized, which is well-known for sensitive detection of light polarization. The first optical element of the bridge is a  $\lambda/2$  plate (half-wave plate), rotating the polarization angle to 45°. The probe beam is subsequently split by a Wollaston prism into its

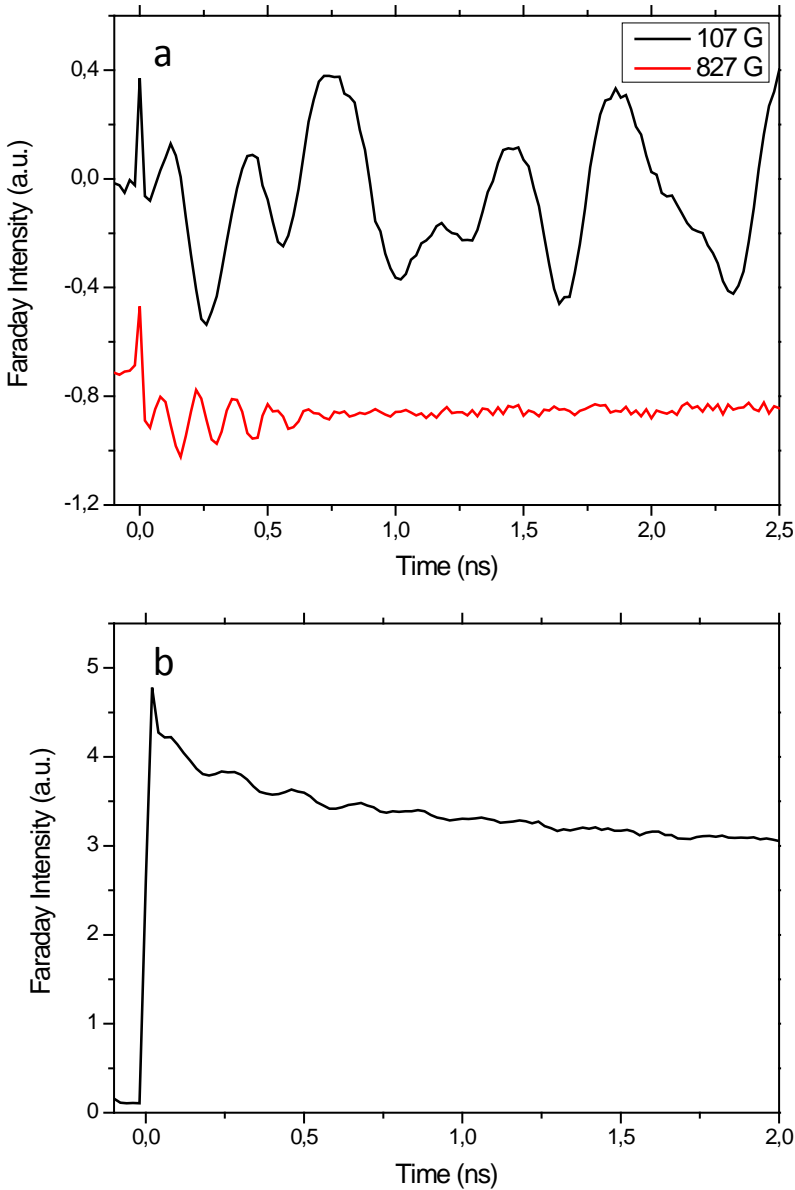


**Figure 2.6:** Sample time traces of Faraday detection. The curves show oscillations with field-dependent frequencies and amplitudes. Intensities can be both positive and negative, corresponding to clockwise and counter-clockwise rotation of the plane of polarization. (a) Nickel sample. Vertically off-set time traces for two different values of applied magnetic field  $H$ . 40 nm nickel on SLG,  $\Lambda = 1.97 \pm 0.02 \mu\text{m}$ . (b) Iron sample at an applied field of  $H = 185$  G, averaged over multiple loops. 10 nm  $\text{Al}_2\text{O}_3$  / 40 nm Fe / 10 nm Al / SLG,  $\Lambda = 1.1 \mu\text{m}$ .

(equally intense) horizontal (H) and vertical (V) polarization component, each of which is subsequently captured by a photodetector. Any small change in polarization will slightly increase the intensity on one of the detectors while causing a small reduction on the other detector, or *vice versa*. The difference signal between the two detectors is then a sensitive measure of the change in polarization angle.

Recording the changes in polarization direction at different delay times results in time traces, of which examples are shown in Figure 2.6. The top panel shows Faraday time traces for a nickel/SLG sample at two different values of applied magnetic field  $H$ . Oscillations are present with a frequency and amplitude that changes with magnetic field, which represent the time-dependent precession of the magnetization vector driven by the underlying elastic waves. For an iron sample, shown in the bottom panel, the oscillations are superposed on a background that is large in comparison to nickel.

## 2.4 Conclusion

This chapter described the general principles of three techniques: the pump-probe technique, the TG geometry and the Faraday detection scheme. All of these techniques are employed in this work in order measure different sample dynamics following pump excitation. The next chapter describes these dynamics, and explains how these phenomena lead to the time traces presented above.

# Chapter 3

## Theory

### 3.1 Sample Excitation

The previous chapter showed representative time traces for the various types of measurements in the transient grating setup. This section gives a theoretical overview of the ultrafast processes involved in TG sample excitation and how these processes lead to the detected curves in the Faraday and TG diffraction channels.

#### 3.1.1 Acoustic Waves and TG Diffraction Detection

It is well known that transient grating spectroscopy involves generation of surface acoustic waves in the sample [18]. Sudden heating of the sample due to optical absorption of the ultrashort pump pulses leads to rapid expansion of the sample surface. At the interference maxima (the ‘hot’ spots) the absorbed energy is larger than at the interference minima (the ‘cold’ spots), causing a spatial modulation of thermal expansion known as a “ripple”. This launches several types of counter-propagating acoustic waves simultaneously, with wavelengths equal to the grating wavelength  $\Lambda$  and propagation velocities depending on the type of acoustic wave and on the mechanical properties of the sample. The counter-propagating acoustic waves result in standing acoustic waves.

The most prominent and well-known acoustic wave that is generated in the TG setup is the Rayleigh Surface Acoustic Wave (SAW). Rayleigh waves are solutions to the wave equation which comprise an imaginary out-of-plane wavevector, and are thus confined to the surface of the sample [19]. They are characterized by nonzero strain components  $\epsilon_{xx}$ ,  $\epsilon_{xz}$  and  $\epsilon_{zz}$ , that attenuate as a function of depth into the sample. Their surface-

bound nature manifests as having long measured lifetimes and do not decay significantly within our maximum time window of  $8\text{ ns}$ . The penetration depth of the Rayleigh wave is in the order of its wavelength. Using thin films with thicknesses much smaller than this wavelength, therefore, the Rayleigh wave propagation velocity depends mostly on the substrate material. In SLG, for example, Rayleigh waves propagate at  $3120 \pm 20\text{ m/s}$  [20].

A second, less well-known, acoustic wave mode is also shown to be generated in our samples, namely the Surface Skimming Longitudinal Wave (SSLW) [20], traveling at  $5590 \pm 15\text{ m/s}$ . These waves are near-surface propagating compressional waves (longitudinal waves), however, to the best of our knowledge, they are not surface-bound waves in the strict sense and do propagate at some shallow angle way from the surface. The experimental observation is then of a rapidly attenuating acoustic waveform on the timescales of a few nanoseconds. The observation of the SSLW was a somewhat unexpected result, in that SSLW generation in the TG configuration has not been previously shown. However, in our TG configuration, all acoustic modes are generated subject to the initial boundary conditions imposed by the thermal stress, and thus it is not unexpected that additional waves are present. A more detailed account on acoustic wave generation due to optical absorption using the transient grating geometry can be found in the literature ([21, 22]).

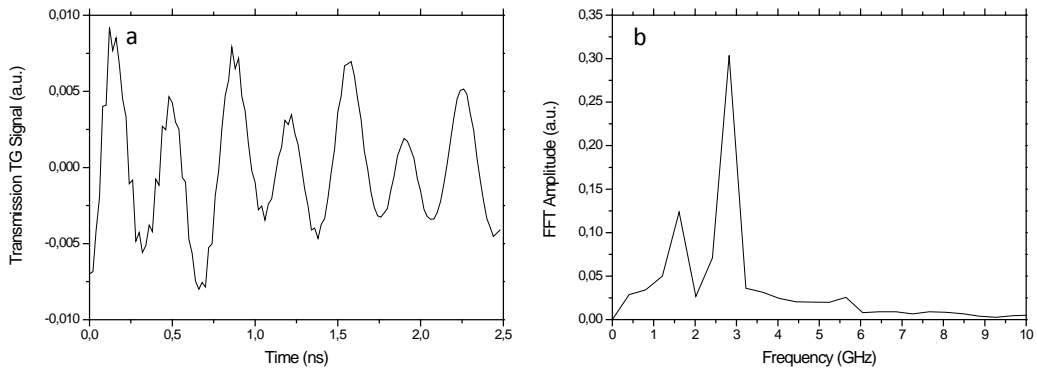


**Figure 3.1:** (a) Same time trace as in Figure 2.5, after background removal. (b) Corresponding (FFT) frequency spectrum, showing two peaks. The lower and higher frequency peaks correspond to the Rayleigh wave and the SSLW respectively.  $40\text{ nm}$  nickel on SLG sample,  $\Lambda = 1.97 \pm 0.02\text{ }\mu\text{m}$ .

Monitoring of the dynamics by looking at the first-order diffracted probe beam results in traces as shown in Figure 2.5. The modulation depth

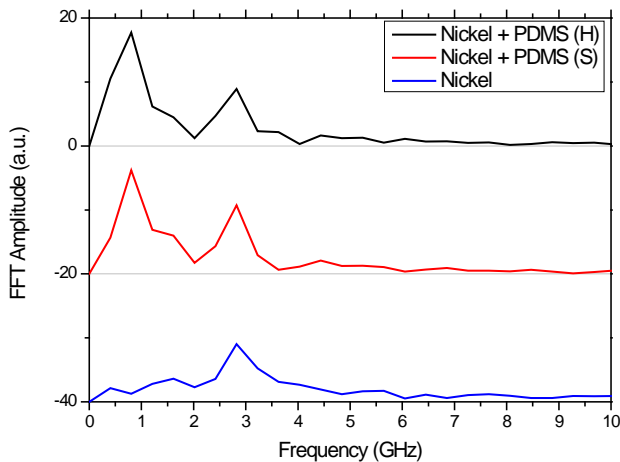


**Figure 3.2:** Frequency spectra of curves shown in Figure 2.5. All three samples show the SSLW frequency. PDMS samples shows an additional peak at lower frequency ( $\approx 1$  GHz). No distinct differences are visible between soft (S) and hard (H) PDMS. All samples include 40 nm nickel on an SLG substrate,  $\Lambda = 1.97 \pm 0.02 \mu\text{m}$ .

of the excited grating changes in time with the frequency of the standing wave, changing the diffraction efficiency for the probe and therefore the intensity on the photodetector. The oscillations present in this ‘TG transmission’ curve are therefore due to the oscillations of the standing acoustic waves. Subtracting the background of the curve and subsequently analyzing the frequency spectra results in the graphs shown in Figure 3.1 and 3.2. Two peaks are clearly visible in the frequency domain for the nickel sample, corresponding to the Rayleigh mode (lower frequency) and the SSLW mode (higher frequency) of SLG. When an additional PDMS layer is deposited on the nickel sample, an extra peak is present at a frequency of  $\approx 1$  GHz. The behaviour is similar for both ‘soft’ (S) and ‘hard’ (H) PDMS. The SAW frequency peak of SLG that is present in Figure 3.1 is less pronounced in Figure 3.2 due to higher noise levels in the time traces. The extra peak at low frequency is indicative of a SAW mode being present inside the PDMS layer, which, due to a lower stiffness coefficient as compared to nickel, is expected to have a lower propagation velocity and therefore a lower frequency. In our time window of 2.5 ns, and using  $\Lambda = 1.97 \pm 0.02 \mu\text{m}$ , the low-frequency response results in approximately one full oscillation period only. Work is currently being done on the installation of a delay stage capable of measuring up to 12 ns of time delay, in order to determine the elastic properties of PDMS more accurately.

### 3.1.2 Magnetoelastic Coupling and Faraday Rotation Detection

The acoustic waves in our TG setup, described in the previous section, couple to the magnetic degrees of freedom via the process of magnetoelastic coupling. Under static conditions, shape anisotropy causes the easy axis of the magnetization to lie in the sample plane, along a minimum  $F^0$  of the magnetic free energy density  $F$ . Launching of the elastic waves due to the pump excitation leads to an additional contribution  $F^{el}$  to the magnetic free energy density, driving  $\mathbf{m}$  away from its equilibrium position [23].  $F^{el}$  depends on the sign and amplitude of the strain  $\epsilon$ . Since  $\epsilon$  is spatially modulated in the  $x$ -direction with wavelength  $\Lambda$ , the resulting magnetization  $\mathbf{m}$  also assumes a spatially periodic form. This magnetoelastic coupling, which is also known as the (inverse) magnetostrictive effect, results in a standing magnetic (spin) wave as schematically depicted in Figure 3.3.

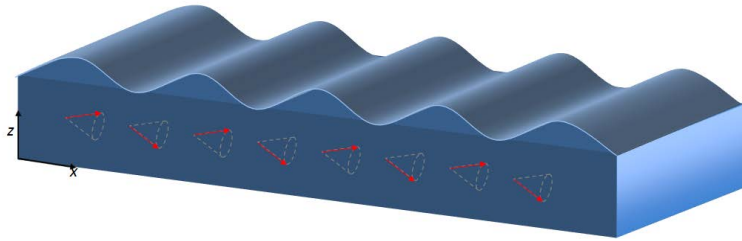


**Figure 3.3:** Schematic representation of the sample showing the ‘ripple’ effect due a strain wave with wavelength  $\Lambda$ . This surface acoustic wave acts as a driving force of a spin wave of equal wavelength due to inverse magnetostrictive effect.

When the magnetization vector  $\mathbf{m} = \mathbf{M}/M$  in an effective magnetic field  $\mathbf{H}_{\text{eff}}$  is brought out of its equilibrium, its subsequent dynamics can be described by the Landau-Lifshitz-Gilbert (LLG) equation,

$$\frac{\partial \mathbf{m}}{\partial t} = -\gamma \mathbf{m} \times \mu_0 \mathbf{H}_{\text{eff}} + \alpha \mathbf{m} \times \frac{\partial \mathbf{m}}{\partial t}, \quad (3.1)$$

where  $\gamma$  is called the ‘gyromagnetic ratio’ and  $\alpha$  is the damping constant. The effective field is dependent on the free energy density,

$$\mathbf{H}_{\text{eff}}(t) = -\frac{1}{\mu_0} \frac{dF(t)}{d\mathbf{M}}, \quad (3.2)$$

and so, through the free energy density, the elastic waves change the effective field  $\mathbf{H}_{\text{eff}}$  in time. For a ferromagnetic thin film with both the external

field  $B_0$  and the magnetization  $M$  lying in-plane, the LLG equation leads to resonance frequencies  $\omega_0$  according to the Kittel formula of ferromagnetic resonance (FMR), *i.e.*

$$\omega_0 = \gamma \sqrt{B_0(B_0 + \mu_0 M)}. \quad (3.3)$$

The  $k = 0$  (and, more generally, long wavelength excitation) spin wave precesses at a field-dependent frequency  $\omega_0$  according to Equation 3.3. The applied field strength can be tuned in such a way that this frequency is equal to the frequency of the acoustic wave, leading to resonant amplification of the acoustic driving of the spin wave. The reader can find more detailed discussion of elastic wave-driven FMR in the literature [12, 23].

Two sample Faraday time traces were provided in Figure 2.6 at different applied fields. The curve at higher field shows a higher frequency as expected in the case of FMR oscillations (Equation 3.3). It is possible to subtract a suitable background function and calculate the frequency spectra in a similar fashion as for the TG diffraction signal. If this process is performed for Faraday time traces at many different magnetic fields (*i.e.* a field scan), it is possible to create a graph as shown in Figure 3.4. The figure shows two horizontal branches corresponding to the frequencies of the SAW (lower branch) and the SSLW (upper branch), both of which are active acoustic modes at all applied fields. When the applied field is tuned in such a way that the FMR frequency matches either the SAW or the SSLW frequency, the magnetic precession dramatically increases in amplitude (as shown in red in the figure). When the FMR is not resonant to any acoustic mode, a signal can still be observed, but the amplitude is low; in Figure 2.6, the 107 G curve is resonant to the SAW and therefore shows large amplitude, while the 827 G curve is not resonant to any elastic mode and therefore has low amplitude and a quick decay rate.

The data presented in Figure 3.4 and 2.6 was obtained using the Faraday detection scheme, which was discussed in Section 2.3. The sample magnetization affects the polarization angle of the probe beam as it passes through the sample due to the so-called ‘Faraday effect’. The Faraday effect is a magnetooptical effect first discovered by M. Faraday in 1845 [24], and states that light undergoes a rotation in polarization plane angle as it traverses a medium that is placed in a magnetic field parallel to the direction of the light beam. The change in polarization angle,  $\beta$ , is linearly proportional to the magnetic field strength  $B$  and the path length  $d$  through the medium:

$$\beta = \nu Bd, \quad (3.4)$$

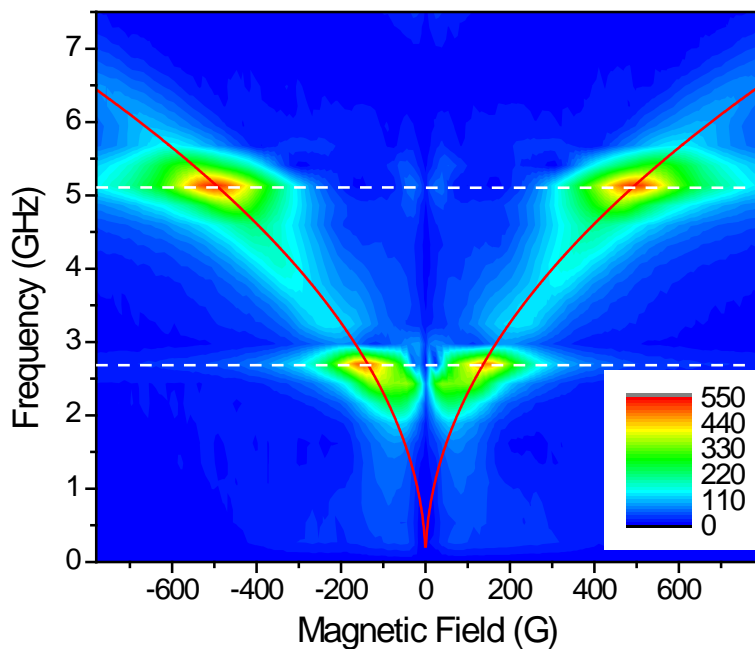


**Figure 3.4:** Graph showing the frequency response of the Faraday signal as a function of in-plane applied magnetic field. The acoustic frequencies are denoted by the dashed white lines, whereas the solid red curves show the frequencies at which ferromagnetic resonance occurs. When the field is tuned such that the corresponding FMR frequency matches one of the acoustic branches, the acoustic mode resonantly drives the magnetic precession to high amplitudes. The upper and lower branch correspond to the SSLW and SAW acoustic mode respectively. 60 nm nickel on SLG sample,  $\Lambda = 1.1 \mu m$ . Figure adapted from [20], to which the author of this thesis has contributed.

where  $\nu$  is the called the ‘Verdet constant’. When the magnetic field is mostly due to the magnetization rather than an externally applied field, the formula can be written in the similar but less familiar form

$$\beta = KM_z d, \quad (3.5)$$

where  $K$  is now the ‘Kundt constant’. The formula contains  $M_z$  rather than  $M$ , as the probe pulse undergoes Faraday rotation due to the magnetization component along the propagation direction - in our setup the  $z$ -direction. We are therefore sensitive to the out-of-plane magnetization component, which can be calculated by measuring the Faraday rotation angle  $\beta$ .

The following calculations are used to quantify the Faraday rotation based on the reading on the two detectors. The intensity of the probe beam is

$$I = |E|^2 = |E_x|^2 + |E_y|^2 \quad (3.6)$$

where  $E$  is the electric field and  $x$  and  $y$  denote the two polarization directions. Initially, the polarization is set at  $45^\circ$  ( $\pi/4$ ), making  $E_x = E_y$ . After a Faraday rotation of  $\beta$  the polarization angle is  $(\pi/4+\beta)$  and  $E_x$  and  $E_y$  become

$$E_x = E \cos\left(\frac{\pi}{4} + \beta\right) = \frac{E}{\sqrt{2}}(\cos(\beta) - \sin(\beta)), \quad (3.7)$$

$$E_y = E \sin\left(\frac{\pi}{4} + \beta\right) = \frac{E}{\sqrt{2}}(\cos(\beta) + \sin(\beta)). \quad (3.8)$$

The photodetector measures the intensity rather than electric field. In the limit of small Faraday rotations, *i.e.*  $\beta \ll 1$ , the measured intensities become

$$I_x = E_x^2 = \frac{E^2}{2}(1 - 2\cos(\beta)\sin(\beta)) \approx \frac{E^2}{2}(1 - 2\beta), \quad (3.9)$$

$$I_y = E_y^2 = \frac{E^2}{2}(1 + 2\cos(\beta)\sin(\beta)) \approx \frac{E^2}{2}(1 + 2\beta). \quad (3.10)$$

Measuring the difference between the two detectors, we get

$$I_{diff} = I_y - I_x = 2E^2\beta = 2I\beta, \quad (3.11)$$

and so the Faraday rotation can be calculated by

$$\beta = \frac{I_{diff}}{2I}. \quad (3.12)$$

## 3.2 The Influence of Temperature on Magnetization Dynamics and its Detection

### 3.2.1 the Two-Temperature Model

Understanding of evolution of the sample temperature is crucial for understanding and interpreting data from the pump probe and Faraday measurements accurately. The dynamics happening within the first few tens of picoseconds can be accurately described by the Two-Temperature Model (TTM), first proposed by Kaganov *et al.* [25] and Anisimov *et al.* [26], where the electrons and the lattice (*i.e.* phonons) are treated as coupled thermodynamic baths that can exchange energy via so-called ‘electron-phonon coupling’. This scheme has been utilized for several decades to describe the thermal dynamics of both electrons and phonons at the early times after optical excitation. The calculation of temperature begins at the instant of optical excitation.

The distance that the laser pulse of wavelength  $\lambda$  penetrates into the sample film can be described by the optical skin depth  $\delta_{skin}$ ,

$$\delta_{skin} = \frac{\lambda}{4\pi\kappa}. \quad (3.13)$$

where  $\kappa$  is the imaginary part of the refractive index of the film material. The intensity and energy of the pulse is given by the Lambert-Beer law:

$$I(z) = I_0 e^{-z/\delta_{skin}}, \quad (3.14)$$

where  $I_0$  is the incident light intensity. The decreasing pulse intensity implies that energy is deposited in the film.

The Two-Temperature Model, which is applicable to metal films only, proposes that the deposited energy is redistributed among electrons and phonons having respective temperatures of  $T_e$  and  $T_i$ . In a metal film, the absorbed photon energy leads to the creation of free electrons (Drude response). In TTM the deposited energy first goes towards instantaneously increasing the temperature  $T_e$  of these free electrons. The thermal energy subsequently transfers from the electrons to the phonons via the process of electron-phonon coupling, until  $T_e = T_i$ , which takes typically less than a few picoseconds. The spatial and temporal evolution of electron and lattice temperatures are calculated by solving the following coupled 1D nonlinear differential equations:

$$\begin{aligned} C_e(T_e) \frac{\partial T_e}{\partial t} &= k(T_e) \frac{\partial^2 T_e}{\partial z^2} - g(T_e - T_i) \\ C_i \frac{\partial T_i}{\partial t} &= g(T_e - T_i), \end{aligned} \quad (3.15)$$

where  $C_e$  is the electronic heat capacity,  $k$  is the electronic thermal conductivity,  $g$  is the electron-phonon coupling constant and  $C_i$  is the lattice heat capacity.  $C_e$  and  $k$  are both dependent on  $T_e$ .

The Two-Temperature Model is used in this thesis to calculate the lattice heat distribution in the magnetic film after excitation. This distribution is then used for the initial conditions, *i.e.* the  $t = 0$  temperature distribution, for the subsequent thermal dynamics of the spatially inhomogeneous temperature profile generated in the TG configuration at the nanosecond scale.

### 3.2.2 Thermal Boundary Resistance

Once the lattice temperature is increased after electron-phonon equilibration, heat will diffuse across the film. When the phonons reach the film/substrate interface, an additional physical quantity comes into play, namely the ‘Thermal boundary resistance’. Thermal boundary resistance, also called ‘Kapitza resistance’  $R_{Kap}$ , is a quantity that becomes important whenever there is heat transfer across an interface between two materials or phases. It was first described by P.L. Kapitza in 1941 [27] when he noticed a discontinuous temperature drop at the interface between liquid and solid helium. It occurs due to interfacial scattering of phonons and electrons and can be described by the formula

$$R_{Kap} = \frac{1}{G_{Kap}} = \frac{\Delta T}{Q}, \quad (3.16)$$

where  $G_{Kap}$  is the thermal boundary conductance,  $Q$  is the heat flux across the boundary and  $\Delta T$  is the accompanying drop in temperature. The larger the value of  $R_{Kap}$ , the longer it takes for heat energy to pass the interface. In the next chapter, the thermal boundary resistance will be determined for nickel/SLG and nickel/MgO interfaces using pump-probe data. The accurate estimate of these values is of importance in this thesis, as it is needed to realistically calculate the temperature dynamics inside the magnetic film.

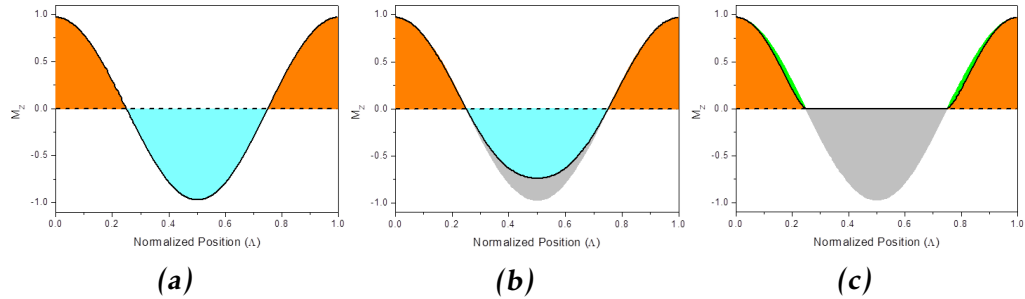


**Figure 3.5:** Illustration of the importance of temperature for determining magnetic contrast, *i.e.* the difference between positive  $M_z$  values (shown in orange) and negative  $M_z$  values (shown in blue) along the spin wave. a) Values of  $M_z$  without taking temperature effects into account. The sum of  $M_z$  is zero; experiment would be insensitive to magnetic dynamics. b) Sensitivity comes from temperature effects due to the pump. ‘Hot’ regions in the grating (between  $0.25\Lambda$  and  $0.75\Lambda$ , blue) become more demagnetized than ‘cold’ regions ( $0-0.25\Lambda$  and  $0.75-1\Lambda$ , orange), leading to non-zero sum. c) At larger fluences the hot regions are completely demagnetized. The magnetization at the cold regions are reduced as well (green regions).

### 3.2.3 Temperature Dependence of Magnetization

The detection of magnetization precession in the transient grating setup is a nontrivial process. It was explained in the previous sections that the application of a grating gives rise to a standing spin wave as well as temperature differences in the sample. The identification of the time-dependent magnetooptic sensitivity in the Faraday detection scheme requires a detailed knowledge of the temperature dynamics following excitation.

With a diameter of approximately  $75 \mu m$ , the probe beam is significantly larger than the grating wavelength  $\Lambda$ , and as such, the probe beam does not measure the value of  $M_z$  at a specific point in the spin wave but rather a value of  $M_z$  integrated over many wavelengths of the spin wave. Within one wavelength,  $M_z$  traverses all precessional phases, and so the averaged value is the sum of both positive and negative  $M_z$ -values (see Figure 3.5). Naively this may lead one to conclude that the average  $M_z$ -value should be zero. During experiments, however, a signal is observed, implying a finite, non-zero average. To elucidate where this sensitivity comes from, a careful analysis of the temperature distributions and dynamics in the sample is performed in the next chapter. To understand why the average value of  $M_z$  is nonzero we must incorporate the temper-

ature differences on the sample. At the positions where the two pump pulses interfere constructively the fluence is high and there is an increase in temperature (a ‘hot’ spot), whereas at the positions of deconstructive interference there is effectively zero fluence and no initial rise in temperature occurs (a ‘cold’ spot). More specifically, the interference pattern of the two pump pulses creates a fluence profile as a function of position  $x$  according to

$$F(x) = 2F_{av} \sin^2\left(\frac{x\pi}{\Lambda}\right), \quad (3.17)$$

where  $F$  and  $F_{av}$  are the fluence and average fluence respectively, and  $\Lambda$  is the grating wavelength.

The nonzero average value for  $M_z$  comes from the fact that the magnetization amplitude  $M$ , and therefore  $M_z$ , depends on temperature. How the temperature affects the magnetization at every point along this profile can be understood using the complete Brillouin expression for the magnetization of spin  $S = \frac{1}{2}$  materials, *i.e.*

$$M = N\mu \tanh(\mu\lambda M/k_B T). \quad (3.18)$$

This equation can be solved numerically and gives nonzero solutions only for  $0 < T < T_c$ . For nickel, with  $T_c = 627$  K, the expression is in good agreement with experimental values [28]. The obtained curve is shown in Figure 3.6.

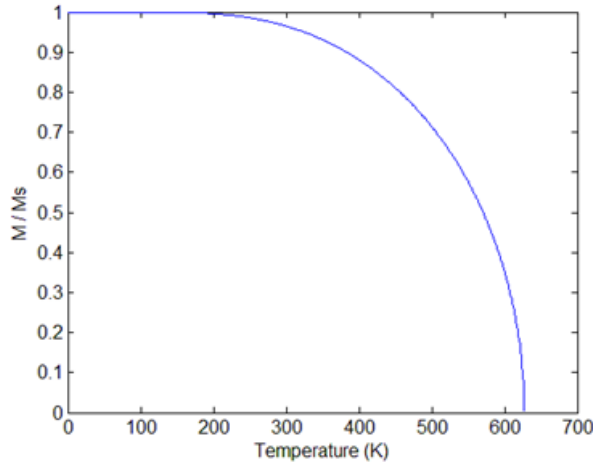


**Figure 3.6:** Temperature dependence of magnetization  $M$ .  $M$  is equal to the saturation magnetization  $M_s$  at absolute zero. At  $T \geq T_c$ , all magnetic ordering is lost ( $T_c = 627$  K for nickel).

All magnetic moments are aligned at absolute zero temperature, and so the magnetization is equal to the saturation magnetization. At increasing temperatures the magnetic moments start to behave increasingly randomly, eventually leading to a completely disordered state with zero magnetization at temperatures of  $T_c$  and above. For nickel at room temperature (300 K),  $M$  is 96.5 % of the saturation magnetization.

The temperature-dependence of magnetization has consequences for the spatial average  $M_z$  value. The spin wave is launched by the grating and therefore has a wavelength equal to the grating wavelength  $\Lambda$ . The  $z$ -component of the magnetic moments at the hot and cold spots therefore always have opposite direction, *i.e.* they are anti-parallel since they are half a wavelength apart. Furthermore, since the temperature is higher at the hot spots, the magnetization there is lower than at the cold spots. This property is at the core of explaining the nonzero average value of  $M_z$ .

If the temperature would be known at every position that is probed - that is, at every x,y,z- coordinate - it is possible to calculate how the magnetization  $M$ , and therefore also  $M_z$ , is affected at every position, with the use of Figure 3.6. By integrating these values we can calculate what percentage of  $M_z$  is observed at the detector. If this is done also for every point in time it is possible to describe transiently this ‘effective’  $M_z$  value. This is the purpose of the next chapter.

### 3.3 Conclusion

The pump-induced interference pattern launches narrow-band acoustic waves, which couple to the magnetic degrees of freedom via the local free energy density, and, consequently, the effective field. This results in a spin wave that precesses at ferromagnetic resonance (FMR) frequencies depending on the externally applied field. Resonant amplification of the FMR response occurs when the magnetic field is tuned in such a way that the frequencies of the elastic wave and the spin wave are equal. Our setup allows us to transiently detect both the elastic waves and the magnetic response, as well as the average temperature dynamics. Spatially resolved temperature dynamics are important for determining the magnetic contrast, and, since this cannot be detected in the TG setup, this has to be established in another way. The next chapter focuses on calculations of magnetooptic sensitivity in the TG setup using numerical analysis.

Chapter **4**

# Temperature Dynamics and Magnetic Contrast of Thin Nickel Films in the Transient Grating setup

## 4.1 Introduction

The magnetic response following TG excitation is observed in real-time using the Faraday detection scheme, which relies on changes in polarization due to the Faraday effect, and which is sensitive only to the average out-of-plane magnetization component (see Chapter 3). In the transient grating geometry, non-zero average values are measured because of temperature inhomogeneities in the sample which cause differences in magnetization amplitude between ‘hot’ and ‘cold’ regions in the film. Knowledge of the spatially-resolved temperature evolution inside the sample allows for quantification of this sensitivity (*i.e.* ‘contrast’), which can be used to estimate the angle at which the standing spin wave precesses, thereby providing a measure of how strongly the magnetic vector is driven out of its equilibrium state by the elastic wave.

In this chapter, a method is presented to calculate the magneto-optic sensitivity in the transient grating geometry as a function of time, using nickel films as a test case. Firstly, the Two-Temperature Model is employed to determine the lattice temperature distribution in a nickel film after pump excitation (Section 4.2). Separately, the Kapitza resistance of nickel/SLG and nickel/MgO interfaces are estimated using experimental

pump-probe data and 1D numerical (finite element) analysis of temperature evolution (Section 4.3). With these boundary conditions, a 2D extension of the model is used to simulate the temperature dynamics of these heterostructures in the transient grating setup (Section 4.4). The resulting spatial and temporal temperature profiles in the nickel film are converted to magnetization dynamics and used to quantify the experimental magnetic contrast, *i.e.* the sensitivity to  $M_z$  as a function of time. An exemplary result is then presented (Section 4.6.1), of which the corresponding ‘contrast curve’ is used to calculate the precessional angle of the standing spin wave. Finally, a discussion follows on how the contrast curve is affected by differences in fluence, sample film thickness, grating wavelength  $\Lambda$ , and substrate material (Section 4.6.2). The results of this chapter have contributed to a paper that is published in *Scientific Reports* [29].

## 4.2 Application of the Two-Temperature Model

The initial lattice temperature distribution due to pump excitation is needed in order to accurately simulate subsequent dynamics. In this study, the initial distribution is obtained by solving the Two-Temperature Model (see Section 3.2.1) numerically. A script was provided by dr. V. Shalagatskyi from the Université du Maine for solving the TTM differential equations (see Equation 3.15). The code uses a Fourier approach to solve for the equilibrium distribution of lattice temperature after ultrafast excitation by a single laser pulse with a specified FWHM temporal width. The relatively slow process of phonon diffusion is not taken into account, as the two temperatures reach equilibrium within a few picoseconds [30]. For a more detailed discussion on the method, the reader is referred to V. Shalagatskyi’s doctoral thesis [30].

The provided code was adapted for application to the case of a single nickel film by selecting appropriate values of  $C_e$ ,  $C_i$ ,  $k$  and  $g$  for application to the case of a single nickel film. The following values were found in the literature and used in the code:  $C_e = 1077.4 \cdot T_e \text{ J m}^{-3} \text{ K}^{-3}$  [31],  $C_i = 3.96 \cdot 10^6 \text{ J m}^{-3} \text{ K}^{-3}$ ,  $k = 90.9 \cdot T_e / T_i \text{ W m}^{-1} \text{ K}^{-1}$  [32] and  $g = 2.3 \cdot 10^{17} \text{ W m}^{-3} \text{ K}^{-1}$  [31].

The output equilibrium lattice temperature distribution for a 40 nm nickel film can be seen in Figure 4.1. The temperature increase  $\Delta T$  as a function of depth  $z$  after two-temperature equilibration can be described well by a simple exponential function:

$$\Delta T(z) = C e^{-z/\alpha} \quad (4.1)$$

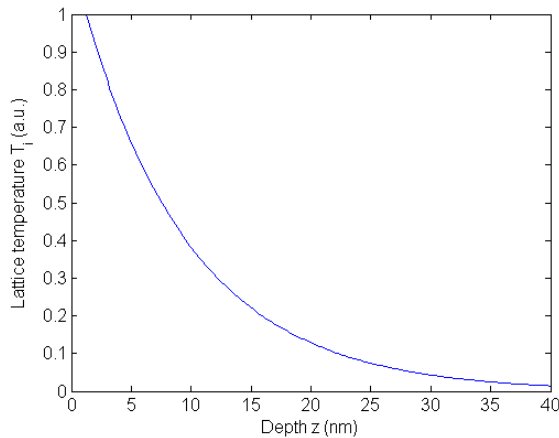


**Figure 4.1:** Increase in lattice temperature as a function of depth ( $z$ ) after equilibration of electrons and phonons, reached within the first few picoseconds after sample excitation, as calculated by the two-temperature model. This distribution is used as initial heat distribution for calculations of subsequent temperature evolution at the nanosecond scale.

where  $\alpha$  specifies the lattice heat depth after two-temperature equilibration, and  $C$  is a scaling constant that depends linearly on pulse fluence. Application of the TTM for the case of a nickel film resulted in  $\alpha = 9.13 \pm 0.01 \text{ nm}$ , which was used throughout all subsequent simulations.

### 4.3 Numerical Simulation of Single Pump Temperature Dynamics - a 1D Model

Since the TTM code includes neither lattice heat diffusion nor the substrate material, finite element modeling software ‘COMSOL Multiphysics®’ (v5.1) is employed to determine the temperature dynamics of the film-substrate heterostructure in the nanosecond regime, following the two-temperature equilibration. In Section 4 the software is explained in detail for a two-dimensional model in order to describe temperature dynamics in the transient grating setup. In this section we are only concerned with single pump excitation, *i.e.* pump-probe data. Single pump excitation is homogenous across the probed sample surface area, and so the temperature is only a function of depth (the  $z$ -dimension). A simple one-dimensional model therefore suffices.

Experimentally, the nickel films are mounted on a transparent sub-

	$k$ $W/(m\cdot K)$	$\rho$ $kg/m$	$C_p$ $J/(kg\cdot K)$
<b>Nickel</b>	90.9[32]	8908	444
<b>SLG</b>	0.92[32]†	2500[33]	870[33]
<b>MgO</b>	49.9[34]	3580	923 [34]

**Table 4.1:** Thermal conductivity ( $k$ ), density ( $\rho$ ) and heat capacity at constant pressure ( $C_p$ ), for nickel, soda lime glass and MgO, used for COMSOL Multi-physics® simulations.

† Approximate silicon contents 60 wt. %.

strate material - usually soda lime glass (SLG) or MgO. Three material properties need to be defined for each of these three materials in order to simulate the heat flow in the structure: the thermal conductivity ( $k$ ), the mass density ( $\rho$ ) and the heat capacity ( $C_p$ , constant pressure). The values of the three quantities for the materials mentioned can be found in Table 4.1.

The temperature dynamics are simulated for a one-dimensional nickel film of 40 nm attached to a 460 nm substrate - thick enough so that the temperature of the backside of the substrate does not increase significantly, thereby avoiding any heat build-up. The resulting temperature evolution for a nickel film of 40 nm on top of a SLG and MgO substrate, using  $R_{Kap} = 0$  and  $R_{Kap} = 3 \cdot 10^{-9} K \cdot m^2 / W$  respectively, is shown in Figure 4.2 (how these values were obtained is explained in the next section).

The initial temperature dynamics, in the first  $\approx 25 ps$ , are very similar for SLG and MgO substrates, as they are mostly determined by the nickel film - very little heat has traveled into the substrate, while the temperature in the film has already reached equilibrium (*i.e.* the temperature in the film is homogeneous). In the subsequent dynamics there are a few key differences between the SLG and MgO sample. Due to the nonzero Kapitza resistance for the MgO case there is a temperature gap at the interface (40 nm). Despite this extra resistance, the temperature of the nickel film drops much faster for the MgO case than for the SLG case. This is due to the much larger thermal conductivity for MgO, causing the heat to travel faster into the depth of the MgO substrate than into the SLG substrate. This can be deduced from the figure as well: even though the temperature of SLG rises faster close the interface, the temperature at the 100 nm mark is significantly higher for MgO (compare, for example, the curves for both substrates at 1 ns).

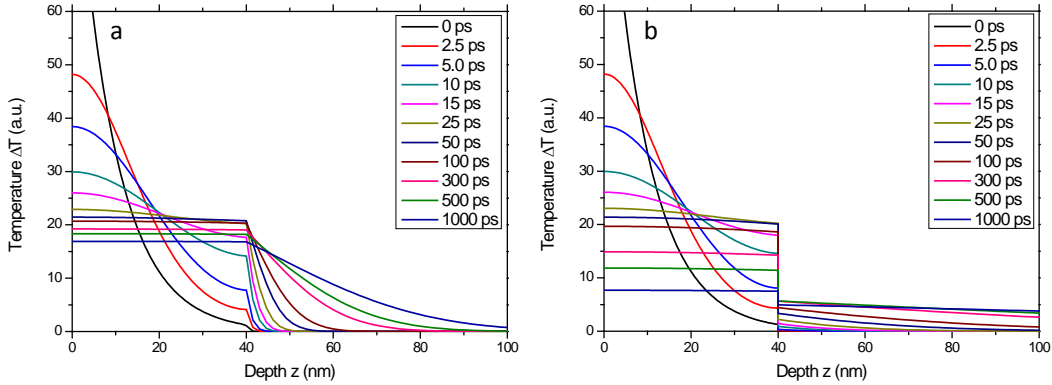


**Figure 4.2:** Evolution of temperature of a 40 nm nickel film on a SLG substrate (a) with  $R_{Kap} = 0$  and on an MgO substrate (b) with  $R_{Kap} = 3 \cdot 10^{-9} \text{ K} \cdot \text{m}^2 / \text{W}$ . The initial temperature distribution, *i.e.* at  $t = 0$ , is equal to the distribution shown in Figure 4.1, which was a result of the TTM approach. Calculations were performed using COMSOL Multiphysics®.

### 4.3.1 Determination of Thermal Boundary Resistance for Nickel/SLG and Nickel/MgO Interfaces

The values for the Kapitza resistances, *i.e.*  $R_{Kap} = 0$  for SLG and  $R_{Kap} = 3 \cdot 10^{-9} \text{ K} \cdot \text{m}^2 / \text{W}$  for MgO, were determined by running the COMSOL Multiphysics® simulation many times for various values for  $R_{Kap}$ , and comparing the result with experimental pump-probe time traces. This comparison was made by plotting the simulated temperature of the film at  $z = 0$  as a function of time. Figure 4.3 shows these plots of the surface temperature for SLG (a) and MgO (b), using various values for  $R_{Kap}$ . Added to these plots is the pump-probe data. It should be noted that the temperatures here are in arbitrary units, and so the data was scaled appropriately. Based on the shape of the curves, an estimation could be made of the correct value of  $R_{Kap}$ .

It can be seen that the experimental data can be fitted remarkably well, justifying the initial proposition that the pump-probe experiment is sensitive to sample temperature. The temperature dynamics are rather different for SLG versus MgO. The observation that was made for Figure 4.2, namely that the (nickel) surface temperature drops at a much quicker rate for MgO than for SLG, can also be made in Figure 4.3. Furthermore, the value of  $R_{Kap}$  has a much larger impact on the shape of the surface tem-

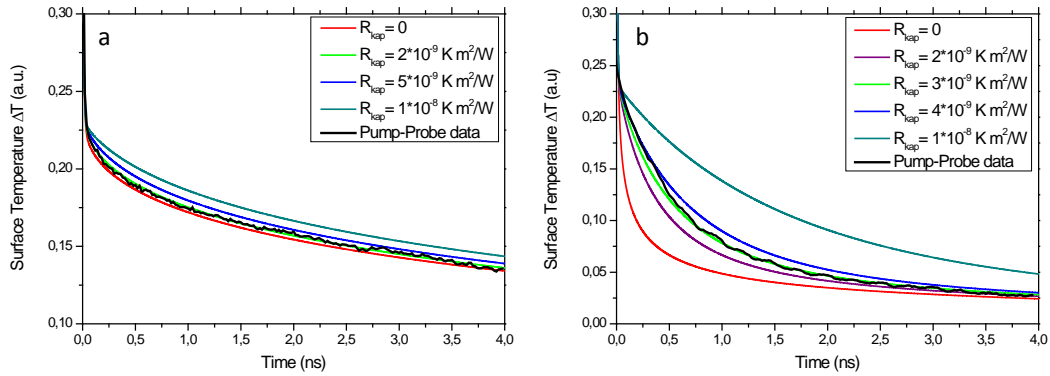


**Figure 4.3:** Experimental pump-probe data (black) of a 40 nm nickel on top of an (a) SLG substrate and (b) MgO substrate, accompanied by surface temperature dynamics calculated using COMSOL Multiphysics® using various values of the Kapitza resistance  $R_{Kap}$ . Correct values of  $R_{Kap}$  for the two types of interfaces are selected on the basis of shape similarity between simulations and experimental data.

perature dynamics of nickel on MgO. This is because for SLG, the added resistance due to  $R_{Kap}$  has a relatively small impact, as the heat diffusion was already obstructed by the much smaller heat conductivity. The shape of the nickel/SLG data is rather similar to the simulated curves with values up to  $R_{Kap} \approx 5 \cdot 10^{-9} \text{ K} \cdot \text{m}^2 / \text{W}$ , which increases the difficulty of determining the correct value of  $R_{Kap}$  for this substrate material with nickel. Using this technique it can only be concluded therefore that the thermal boundary resistance between nickel and SLG is  $0 < R_{Kap} < 5 \cdot 10^{-9} \text{ K} \cdot \text{m}^2 / \text{W}$ . The importance of the Kapitza resistance in this research is to assure accurate simulations of the thermal diffusion. Because for SLG the exact value of  $R_{Kap}$  is not crucial for the dynamics, a value of  $R_{Kap} = 0$  was used throughout the simulations of nickel on SLG for simplicity.

The correct value of  $R_{Kap}$  is easier to determine for the nickel/MgO interface. The shape is clearly affected by  $R_{Kap}$ , and from Figure 4.3 it can be concluded that simulations using  $R_{Kap} = (3 \pm 1) \cdot 10^{-9} \text{ K} \cdot \text{m}^2 / \text{W}$  accurately describe the temperature diffusion. This value was therefore used in the simulations of samples of nickel on MgO substrates.

## 4.4 Numerical Simulation of Transient Grating Temperature Dynamics - a 2D Model

### 4.4.1 Sample Dimensions and Meshing

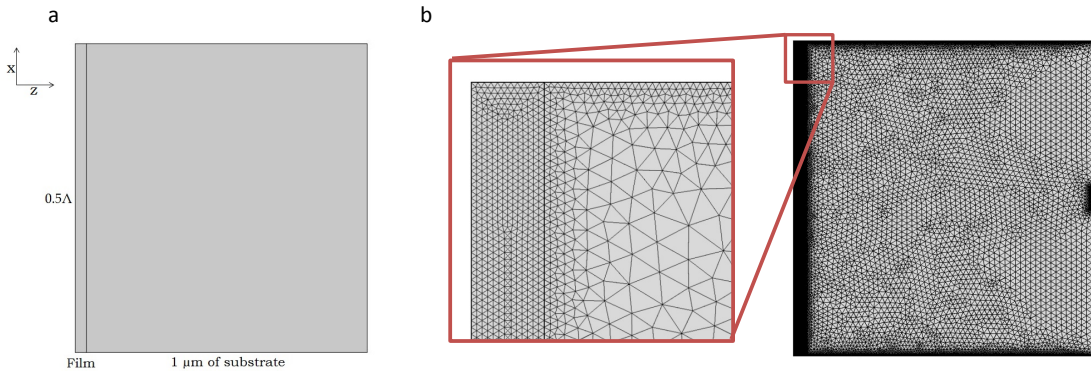


**Figure 4.4:** (a) Structure and dimensions of the sample in COMSOL. (b) Meshing of the sample; the temperature is evaluated by COMSOL at all nodes for every time step. The magnetic film is meshed more densely as it is of greater importance for subsequent calculations of magnetization dynamics.

The temperature distribution in the transient grating setup is not homogeneous across the probed sample surface: it changes periodically as a function of the lateral ( $x$ -)dimension. A 2D model is therefore needed to simulate the temperature dynamics (*i.e.*  $T = T(x, z)$ ). The structure that was used for all 2D simulations is shown in Figure 4.4.

The size of one grating wavelength  $\Lambda$  ( $0.5\text{--}10 \mu\text{m}$ ) is much smaller than the diameter of the probe beam ( $\approx 75 \mu\text{m}$ ), which in turn is much smaller than the entire applied grating pattern ( $\approx 150 \mu\text{m}$ ). It is therefore assumed that the temperature distribution within the probed area is periodic in space, *i.e.*  $T(x) = T(x + \Lambda)$ . This means that if the distribution of temperature is known within one grating period, it is known within the entire probed area.

The temperature profiles, since they are periodic in nature, contain two symmetry-axes per grating period, namely at every temperature maximum and at every temperature minimum. It is possible to ‘cut’ the simulated sample at every symmetry axis, without loss of information. At these maxima and minima, the temperature gradient is pointing along the  $z$ -axis, *i.e.* heat at these locations will not move transversely but only into the sample thickness. Since no thermal energy will be exchanged between

two points separated by symmetry axis, it is unnecessary to simulate beyond any of these symmetry axes. A prerequisite is however that at the boundaries of the sample either a minimum or a maximum is located. The most efficient model is then to model half a grating period, starting at a minimum and ending at a maximum (or *vice versa*).

Little heat travels to the backside of the SLG and MgO substrates within the time-frame of the experiment ( $8\text{ ns}$ ). A substrate thickness of  $1\text{ }\mu\text{m}$  was chosen as it led to sufficiently short computation times while avoiding significant energy build-up at the backside of the substrate.

A mesh has to be created to define the coordinates at which the temperature is calculated by the software. The (triangular) mesh used for the structure is shown in Figure 4.4. The magnetic film was meshed more finely than the inner regions of the substrate, as we are more interested in the temperature distributions inside the film. At a later stage, the temperatures inside the film are used to calculate the magnetization dynamics. It can be noticed that the upper and lower boundary in the figure are meshed finely as well. This has no significance, and is due to the manner in which COMSOL defines the nodal points.

#### 4.4.2 Initial Temperature Distribution

The pump pulses travelling in the z-direction create a sinusoidal temperature grating on the sample with the wavevector  $\mathbf{k}$  pointing in the x-direction. In the z-direction the temperature profile assumes the exponential form as shown in Figure 4.1. The full thermal profile at  $t = 0$  can therefore be written as

$$T(x,z) = (T_{max} - T_{amb}) e^{-z/\alpha} \sin^2\left(\frac{\pi x}{\Lambda}\right) + T_{amb}, \quad (4.2)$$

where  $T_{max}$  is the temperature at a hot spot at the surface,  $T_{amb}$  is the ambient temperature, and  $\alpha = 9.13 \pm 0.01\text{ nm}$ .

The value for  $T_{max}$  can be calculated when the fluence profile  $F$  is known. The pump beam is assumed to have a Gaussian cross-section profile:

$$F = F_0 e^{\frac{x^2}{2\sigma_x^2} + \frac{y^2}{2\sigma_y^2}} \quad (4.3)$$

where  $\sigma_x$  and  $\sigma_y$  are the Gaussian RMS width in the x- and y-direction respectively. The probe beam, being significantly smaller than the pump, is positioned in the middle of the pump beam, and so probes the spot where the fluence attains its maximum, *i.e.* where  $F \approx F_0$ . The simulation

therefore assumes a constant fluence equal to  $F_0$ . The total pump pulse energy is equal to the integral of the fluence over all space.  $F_0$  can be calculated with the use of the following identity of Gaussian functions:

$$E_{pump} = \int_{-\infty}^{\infty} \int_{-\infty}^{\infty} F \, dx \, dy = F_0 2\pi \sigma_1 \sigma_2, \quad (4.4)$$

and so

$$F_0 = \frac{E_{pump}}{2\pi \sigma_1 \sigma_2}. \quad (4.5)$$

$E_{pump}$  varies per experiment, and is measured experimentally using a power meter, taking into account the pulse repetition rate of the laser. The values  $\sigma_1$  and  $\sigma_2$  of the pump pulse area were determined once by taking a photograph of the pump beam with a CCD camera and fitting the measured light intensity on the sensor with a 2D-Gaussian. This method provided values of  $\sigma_1 = 165.81 \pm 0.04 \mu\text{m}$  and  $\sigma_2 = 122.67 \pm 0.03 \mu\text{m}$ .

If it is assumed that all pump energy is deposited into the film, so that there is no transmission,  $T_{max}$  can be determined by recognizing that the following equation must hold for the heat energy  $E_{grat}$  across one grating period:

$$\begin{aligned} E_{grat} &= (1-R)F_0\Lambda y + \rho C_p T_{amb} \Lambda y d \\ &= \rho C_p y \int_0^d \int_0^\Lambda \left( (T_{max} - T_{amb}) e^{-z/\alpha} \sin^2\left(\frac{\pi x}{\Lambda}\right) + T_{amb} \right) dx dz, \end{aligned} \quad (4.6)$$

where  $R$  is the reflectivity of the nickel film and  $d$  the film thickness. For a nickel film with thicknesses in the range that is used for the experiments (40-80 nm) this is a reasonable approximation - a nickel film of 40 nm has an internal transmission of 0.05 [35]. Taking (multiple) reflections into account further reduces the net transmission. The current model is therefore however not suitable for very thin nickel films, in which case it would be more appropriate to expand the model to incorporate light transmission.

Evaluation of the integral in equation 4.6 yields

$$E_{grat} = -\alpha \rho C_p y (T_{max} - T_{amb}) \left[ e^{-\frac{d}{\alpha}} \right]_0^d \left[ \frac{x}{2} - \frac{\Lambda \sin\left(\frac{2\pi x}{\Lambda}\right)}{4\pi} \right]_0^\Lambda + T_{amb} d \Lambda. \quad (4.7)$$

Equating expressions 4.6 and 4.7,  $T_{max}$  becomes

$$T_{max} = \frac{2(1-R)F_0}{\alpha\rho C_p[1-e^{-\frac{d}{\alpha}}]} + T_{amb}. \quad (4.8)$$

The initial temperature distribution is found by substituting the result for  $T_{max}$  into equation 4.2.

#### 4.4.3 Physics Applied to the Model

The temperature dynamics are calculated by COMSOL Multiphysics® using the following form of the time-dependent partial differential heat equation:

$$\rho C_p \frac{dT}{dt} = \nabla \cdot (k \nabla T) + Q. \quad (4.9)$$

$T$  is defined by 4.2, the values used for  $\rho, C_p$  and  $k$  are shown in Table 4.1. The heat equation is evaluated at the nodes of the mesh up to 8 ns - the experimental time window - with a time step of  $\Delta t = 5 ps$ , resulting in a total computational time of approximately 2 minutes.

Kapitza resistance is also incorporated for the case of the MgO substrate. A value of  $3 \cdot 10^{-9} K^2/W$  was used, as determined in Section 4.3.  $R_{Kap}$  was found to be negligible for nickel on SLG samples.

In a time span of 8 ns no significant heat flux from the sample into the air is assumed, and is therefore not taken into account by the current model. Heat energy loss into the environment could be incorporated for more accuracy, in which case the Kapitza resistance between nickel and air should be determined as well.

### 4.5 Determination of Magnetization Dynamics and Magnetooptic Sensitivity

The values of  $M_z$  in the standing spin wave are modulated by a (spatial) cosine (see Figure 3.5a). This cosine is of the form

$$M_z(x, t) = M_{z,0} \cos\left(\frac{2\pi x}{\Lambda}\right) e^{-i\omega t} \quad (4.10)$$

The amplitude is however also modulated due to the thermal profile. The magnetization amplitude at every  $(x,z,t)$ -coordinate is calculated by multiplying by a factor of  $m(x, t) = M(x, t)/M_s$ . This factor  $m$  modulates

all components of  $M$ , including the out-of-plane  $M_z$ -component. Combining the thermal effects and the spatially periodic modulation, the complete  $M_z$ -profile can therefore be written as

$$M_z(x, t) = M_{z,0} m(x, t) \cos\left(\frac{2\pi x}{\Lambda}\right) e^{-i\omega t}. \quad (4.11)$$

The Faraday detection scheme is sensitive to  $\langle M_z(t) \rangle$ , which equals all  $M_z$ -values integrated over a full grating period. Its size relative to the actual  $M_z$ -value is then given by

$$\eta = \frac{\langle M_z(t) \rangle}{M_{z,0}} = e^{-i\omega t} \int_0^{\Lambda} m(x, t) \cos\left(\frac{2\pi x}{\Lambda}\right) dx \quad (4.12)$$

The importance of  $\eta$  is that it represents the magnetooptical sensitivity, also called the ‘magnetooptical contrast’ or simply ‘contrast’ throughout this report. If  $\eta = 0.1$  at a certain point in time, it means that the value  $\langle M_z(t) \rangle$  measured experimentally is a factor of 10 lower than the actual (‘real’) value of  $M_z$ . To retrieve the true  $M_z$ -value, the measured  $\langle M_z(t) \rangle$ -value should then simply be multiplied by a factor of 10 (*i.e.* divided by  $\eta$ ).

The value  $\eta$  is obtained using Matlab in three steps. Firstly, the absolute temperatures obtained during the COMSOL simulations are converted into reduced magnetization amplitudes  $M_z/M_{z,s}$  at every  $(x, z, t)$ -coordinate, with the use of the curve shown in Figure 3.6. Secondly, the reduced magnetization amplitudes are multiplied by a cosine as shown in Figure 3.5a. Lastly, the resulting values of  $M_z$  are averaged to arrive at the value of  $\langle M_z(t) \rangle$ . A contrast curve  $\eta(t)$  is generated by calculating  $\eta$  at every point in time.

The careful reader may have noted that the factor  $e^{-i\omega t}$  is omitted. To simplify the procedure, and because the temporal frequency  $\omega$  and phase are not *a priori* known precisely, the factor  $e^{-i\omega t}$  is set to unity, *i.e.* the absolute value is used. During the experiment,  $\langle M_z(t) \rangle$  is modulated by  $e^{-i\omega t}$ , and as a result, these oscillations are not taken into account using the described procedure.

## 4.6 Results: Temperature, Magnetization and Contrast Dynamics

### 4.6.1 Discussion of an Exemplary Result

For illustration purposes, this subsection provides a typical result from the COMSOL Multiphysics® simulations and subsequent post-processing in Matlab, by means of a sample dataset (nickel film thickness  $d = 40 \text{ nm}$  on SLG, fluence  $F_0 = 3.5 \text{ mJ/cm}^2$ , grating wavelength  $\Lambda = 1.1 \mu\text{m}$ ).

Figure 4.5 shows the result of the COMSOL simulation steps for the sample dataset at three different points in time (left-hand subfigures), together with their conversion into reduced magnetization values (right-hand subfigures). The temperature is shown up to a depth of  $160 \text{ nm}$  (*i.e.* the film of  $40 \text{ nm}$  plus  $120 \text{ nm}$  of the glass substrate), while the magnetization distributions are shown only for the nickel film (up to  $40 \text{ nm}$ ) as the substrate is nonmagnetic. The magnetization phase is not incorporated yet into this figure. Also note that the color scale bars are different for each panel. A short discussion for each of the three time slices follows below.

#### **t = 0 ps**

The largest temperatures at this initial time are located close to the outer nickel film surface and at the ‘hot’ spot. The maximum temperature for this simulation is  $1290 \text{ K}$ , significantly larger than the Curie temperature ( $T_c = 627 \text{ K}$ ). This is reflected in the magnetization distribution: a sizable part of the film is completely demagnetized. The sharp edge of the curve shown in Figure 3.6 causes a distinct rapid increase of magnetization just outside the demagnetized region. Using higher fluences, temperatures may reach values exceeding the  $1728 \text{ K}$  nickel melting point. The significance of this is not explored in this thesis.

#### **t = 35 ps**

Within the first  $35 \text{ ps}$  the temperature has almost completely equilibrated along the sample thickness. Lateral diffusion up to this point is less pronounced since the length scales involved are much larger than the film thickness ( $\Lambda = 1.1 \mu\text{m}$  compared to  $d = 40 \text{ nm}$ ). Almost no temperature increase of the substrate has occurred due to the significantly smaller thermal conductivity of SLG than nickel (see Table 4.1).

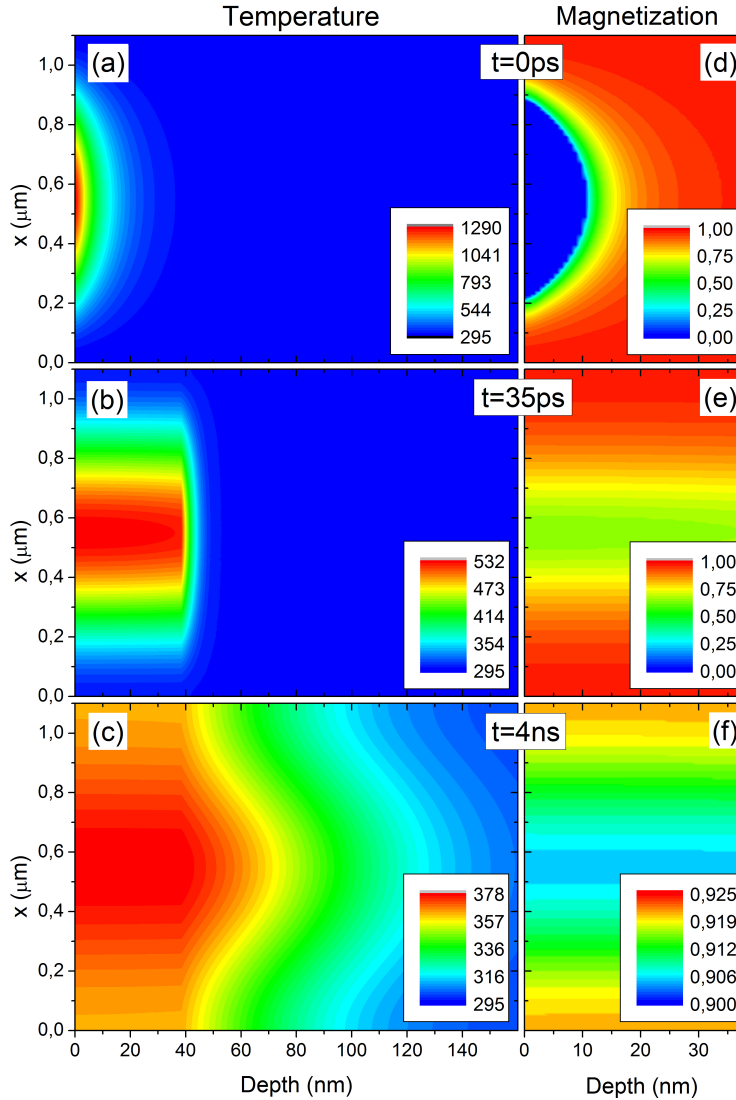


**Figure 4.5:** Calculation of the time-dependent magnetic contrast requires a detailed knowledge of the temperature dynamics and the resulting magnetization amplitude. Panels (a) - (c) show the distributions of temperature at three different times,  $t = 0 \text{ ps}$ ,  $35 \text{ ps}$ , and  $4 \text{ ns}$ . The initial distribution ( $t = 0 \text{ ps}$ ) shows the thermal profile after electron-phonon equilibration according to the two-temperature model (typically  $< 2 \text{ ps}$  after pump pulse excitation), while subsequent thermal diffusion is calculated using COMSOL Multiphysics® simulations. Note that the horizontal and vertical length scales have different units. Panels (d) - (f) show the corresponding spatial distributions of the reduced magnetization  $M/M_s$ , calculated using Matlab, where unity represents the magnetization at  $T = 0 \text{ K}$ . Fluence  $F_0 = 3.5 \text{ mJ/cm}^2$ , film thickness  $d = 40 \text{ nm}$ , grating wavelength  $\Lambda = 1.1 \mu\text{m}$ . For an animated representation of the full temperature and magnetization dynamics at two different fluences, please visit [36] and [37].

Furthermore, within these initial 35 ps the maximum temperature has dropped below  $T_c$  and is now equal to 532 K. As a consequence there are no fully demagnetized regions. The lowest value for the reduced magnetization is now  $M/M_s = 0.62$ . This dramatic difference from the initial magnetization distribution is (again) due to the sharp edge in Figure 3.6.

### **t = 4 ns**

Lateral diffusion and heat flow into the substrate have become significant within the first few nanoseconds. The temperature difference between the hot and cold spots in the nickel film has dropped below 15 K, with a maximum temperature of 378 K. The magnetization profile has become significantly more uniform, with a difference of less than 0.02 between the most demagnetized and least demagnetized regions.

The contrast curve  $\eta$  is obtained by multiplying the magnetization distribution with the cosine function to account for the phase, and subsequently calculating the average value (see Section 4.5 for more details on the procedure). The contrast curve shown in Figure 4.6 was generated by doing this for every time slice of the simulation.

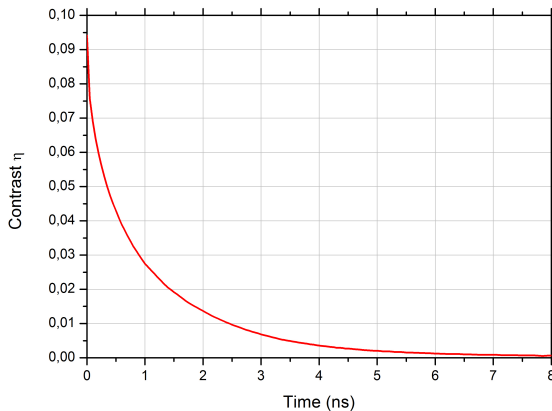


**Figure 4.6:** Contrast curve for the sample dataset. At early times, demagnetization of the hot spot gives rise to magneto-optical sensitivity: at  $t = 0$ ,  $\eta \approx 0.1$ , which means that the measured  $M_z$  amplitude is a factor 10 lower than the actual  $M_z$  amplitude. Subsequent lateral diffusion and overall cooling of the sample reduces the difference in magnetization between the hot and cold spots, thereby decreasing the contrast.

Even though the shape of the contrast curve highly depends on the various parameter, as we shall see in Sections 4.6.2-4.6.2, it is still appropriate to discuss some general features.

It can be noted that  $\eta$  is generally quite low. The lower the value of  $\eta$ , the less visible  $M_z$  is experimentally. In this specific contrast curve, the sensitivity to  $M_{z,0}$  starts at a value of  $\eta = 0.094$ , *i.e.* the experimentally measured  $M_z$  amplitude is 9.4 % of the actual, ‘real’,  $M_z$  amplitude. The theoretical maximum sensitivity is attained in the hypothetical case of a fully demagnetized hot region and a fully magnetized cold region (or *vice versa*), so that there is no mixture of positive and negative  $M_z$  values. By integrating over a full grating period  $\Lambda$ , one then arrives at a theoretical upper limit of  $\eta_{max} = 1/\pi \approx 0.31$ .

The contrast curve can be roughly divided in two stages. The first stage takes up the times from  $t = 0$  to  $t \approx 35\text{ ps}$ , and so is barely visible in the  $8\text{ ns}$  window. This stage is dominated by the quick temperature equilibration across the nickel film. These fast changes are accompanied by changes in magnetization, causing a fast jump in  $\eta$  in this early time period.

The second stage starts once the temperature has equilibrated across the thin film, *i.e.* at  $t \gtrsim 35\text{ ps}$ . It is dominated by the lateral heat diffusion in the film and heat dissipation into the substrate. This process takes more time in general and results in slower changes in  $\eta$ . Eventually, as  $t \rightarrow \infty$ , the initial hot and cold spots attain a temperature equilibrium, and there is no contrast left ( $\eta = 0$ ).

The Faraday time traces can be corrected by dividing every value of the curve by the corresponding value  $\eta$  on the contrast curve. A resulting corrected time trace of an SSLW-resonant Faraday measurement is shown in Figure 4.7.

The original and corrected curve exhibit a few differences, the most obvious being the much larger amplitudes. This is due the small values of  $\eta$ , especially at later times. Additionally, in the original data set the spin wave seems to reach its maximum amplitude at  $t \approx 0.6\text{ ns}$ , whereas the corrected curve shows amplitude growth up to  $t \approx 1.0\text{ ns}$ . Furthermore, the subsequent decay occurs much faster for the original data than the corrected data. Although the data set originally extended to  $8\text{ ns}$ , the graph only shows the first  $4\text{ ns}$  due to increases in noise levels at later times.

## Calculation of Precessional Angle

The corrected time trace provides an opportunity to estimate the precessional angle of the standing spin wave. The curve attains its largest absolute value for the Faraday rotation at time  $t = 1.00\text{ ns}$  with a corrected

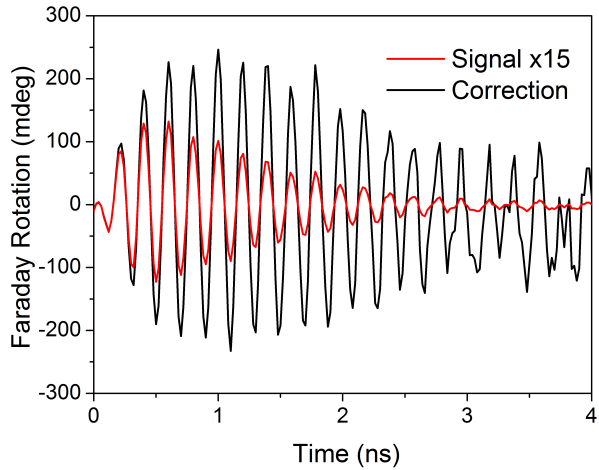


**Figure 4.7:** The corrected curve (black) calculated from the original Faraday data set resonant with the SSLW excitation (red). The original curve is multiplied by a factor of 15 for visibility.

polarization rotation of  $\theta = 247 \text{ mdeg}$ . The corresponding magnitude of  $M_{z,0}$  at this point can be calculated using Equation 3.5 with  $K = 4.0 \cdot 10^{11} \text{ mdeg} \cdot \text{m}^{-1} \cdot T^{-1}$  [38] :

$$M_{z,0} = \frac{\theta}{Kd} = \frac{247}{4.0 \cdot 10^{11} \cdot 40 \cdot 10^{-9}} = 0.015 \text{ T} \quad (4.13)$$

Using a saturation magnetization of  $M_s = 0.051 \text{ T}$  [38] an estimation of the precessional angle  $\alpha$  can be made:

$$\alpha = \arcsin\left(\frac{M_{z,0}}{M_s}\right) = \arcsin\left(\frac{0.015}{0.051}\right) = 17 \text{ deg.} \quad (4.14)$$

Since thin films exhibit an in-plane easy magnetization axis, the precessional motion is elliptical rather than circular, with the major axis of the ellipse parallel to the film. The angle calculated above is based on the out-of-plane magnetization, and gives therefore an estimation of the (smaller) out-of-plane magnetization precession angle. The error in the calculated value of  $\alpha$  is difficult to determine as it relies on complex computer simulations with various assumptions, and therefore the obtained angle should be verified via a different route. Transducer-based elastically driven magnetic wave have reported precessional angles all the way up to  $180^\circ$  [39]. Compared to this, the spin waves in our film precess at a rather modest angle. Optically excited picosecond acoustic pulses, however, have been reported in the literature to drive magnetization precession angles in

the order of  $\approx 0.1^\circ$  [14]. The transient grating geometry therefore greatly enhances the precessional reach of optically-based magnetoelastic generation of spin waves.

#### 4.6.2 Influence of Fluence, Film Thickness, Grating Wavelength, and Substrate Material on Magnetooptic Sensitivity

##### Fluence Dependence

The shape of the contrast curves is highly dependent on fluence ( $F_0$ ). Figures 4.8a,b show the results of contrast dynamics with varying fluence while keeping all other parameters constant during the simulations. Figure 4.8c depicts the temperature at the hot spots ( $x = 0.5\Lambda$ ) and cold spots ( $x = 0$ ) for three selected fluences, averaged over the film thickness  $d$ .

The value of  $\eta$  depends on the contrast (or difference) between the magnetization at the cold spots and the hot spots. For low fluences, such as  $0.5 \text{ mJ/cm}^2$ , the hot spots do not come close to the Curie Temperature  $T_c$ . No significant demagnetization occurs in the sample and therefore the contrast is very small.

For a fluence of  $2.5 \text{ mJ/cm}^2$  the initial temperature at the hot spot is large enough to cause a contrast of  $\eta = 0.07$ . The maximum temperature at  $t = 0$  for this fluence is  $980 \text{ K}$ , significantly larger than  $T_c$ . Temperature equilibration across the thickness of the film reduces this maximum temperature to  $456 \text{ K}$  within the first  $\approx 35 \text{ ps}$ . Magnetization of the hot spot increases rapidly as its temperature drops below  $T_c$  (see Figure 3.6), reducing the contrast.

At  $5.0 \text{ mJ/cm}^2$  the maximum temperature remains above  $T_c$  even after equilibration across the film thickness. At  $t = 0$  the part of the film close to the surface is heated up to a temperature of  $1662 \text{ K}$ . At  $t = 35 \text{ ps}$  the heat has distributed across the thickness, leaving an average temperature of  $627.2 \text{ K}$ , just above  $T_c$ . The resulting decrease of magnetization at the hot spots results in an initial upward jump in contrast. Following these early dynamics is lateral diffusion and diffusion into the substrate. Evidence of lateral diffusion can be seen in Figure 4.8c by observing that the difference in temperature between the hot and cold spots is reducing over time, *i.e.* the temperatures approach each other. Diffusion into the substrate results in an overall cooling of the nickel film which is also visible in the figure. The cooling of the sample combined with the lateral diffusion results in remagnetization of the hot region, accompanied by a gradual decrease in contrast.

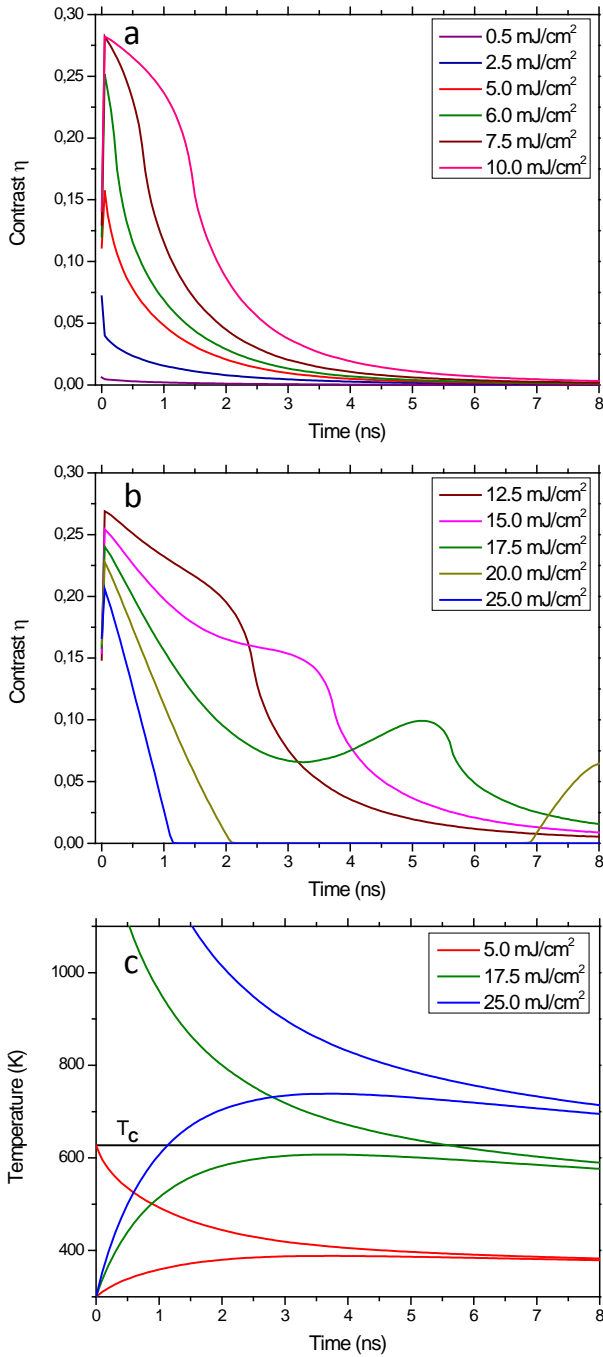


**Figure 4.8:** (a) and (b): Contrast curves for various fluences (split over two panels for clarity). The corresponding temperature dynamics are shown for three selected fluences in panel (c). Each fluence is represented by two film temperature curves: the temperature at the ‘hot’ spot (downward curves) and ‘cold’ spot (starting at room temperature at  $t = 0$ ), averaged over the film thickness. Film thickness  $d = 40 \text{ nm}$ , grating wavelength  $\Lambda = 1.1 \mu\text{m}$ , SLG substrate.

Higher fluences of up to  $12.5 \text{ mJ/cm}^2$  are characterized by contrast curves similar in shape to the  $F_0 = 5.0 \text{ mJ/cm}^2$  curve. The contrast is larger because a larger portion of the hot region (between  $x = 0.25\Lambda$  and  $x = 0.75\Lambda$ , see Figure 3.5) is completely demagnetized. A formation of a ‘shoulder’ can be observed in the contrast curves. The point where  $\eta$  reduces the fastest, at the inflection point, corresponds to the moment at which the maximum temperature (of the hot spot) passes through  $T_c$  and the hot region remagnetizes.

Above  $F_0 = 12.5 \text{ mJ/cm}^2$  the contrast curves become more complex, containing two inflection points. For  $15 \text{ mJ/cm}^2$  and above the formation of a distinct ‘bump’ becomes evident. This fluence regime is characterized by cold spot temperatures approaching or exceeding  $T_c$ . A discussion of the various stages of contrast curves of this type is appropriate. The initial equilibration results in lowered values of  $\eta$  for increasing fluence. The reason for this is that not only the hot region is demagnetized, but also the cold regions become partially demagnetized. This reduces the contrast between the two regions, compared to the lower fluences. Subsequent lateral diffusion heats the cold region and demagnetizes it even further, decreasing the contrast. Ongoing cooling of the film due to diffusion into the substrate causes the heating of the cold region to slow down. The cold region reaches a maximum temperature of  $607 \text{ K}$  for  $F_0 = 17.5 \text{ mJ/cm}^2$  (green curves) at  $t \approx 3 \text{ ns}$ . After this time the cold region remagnetizes as it becomes colder again, while the hot region remains in a demagnetized state. This causes an increase in contrast, resulting in the formation of a ‘bump’. At  $t \approx 5.5 \text{ ns}$  the maximum temperature of the hot region drops below  $T_c$  and quickly remagnetizes as well. After this point, the contrast curve develops in much the same way as the lower fluence cases, characterised by a gradual decrease of  $\eta$ .

In the high-fluence regime -  $F_0 > 17.5 \text{ mJ/cm}^2$  - the coldest points of the film reach temperatures surpassing the Curie temperature at certain times. The film is then entirely demagnetized, and  $\eta = 0$ , as there is nothing to measure. The blue curves in Figure 4.8 show the dynamics of  $F_0 = 25.0 \text{ mJ/cm}^2$ . A nonzero contrast exists until the temperature of the cold region grows larger than  $T_c$  at  $t \approx 1 \text{ ns}$ , after which  $\eta = 0$ . Once the temperature of the cold spot drops below  $T_c$ , a sudden increase in  $\eta$  results, visible for example at  $t \approx 7 \text{ ns}$  for the  $20.0 \text{ mJ/cm}^2$  curve. For  $F_0 = 25 \text{ mJ/cm}^2$  this event does not occur within the time window of  $8 \text{ ns}$ .

The fluence dependence confirms what was already noticed during the experiments, namely that the pump intensity has to be chosen carefully in order to measure the largest signals. Even though the simulations provide a way to correct the measured data, the signal, and therefore  $\eta$ , should

always be maximized during the experiment in order to reduce the signal-to-noise ratio. For example, a fluence in the range of  $F_0 = 10.0 - 15.0 \text{ mJ/cm}^2$  is advised for nickel samples on an SLG substrate with a film thickness of  $d = 40 \text{ nm}$  and a grating wavelength of  $\Lambda = 1.1 \mu\text{m}$ , as it leads to the largest overall values of  $\eta$ .

### Film Thickness Dependence

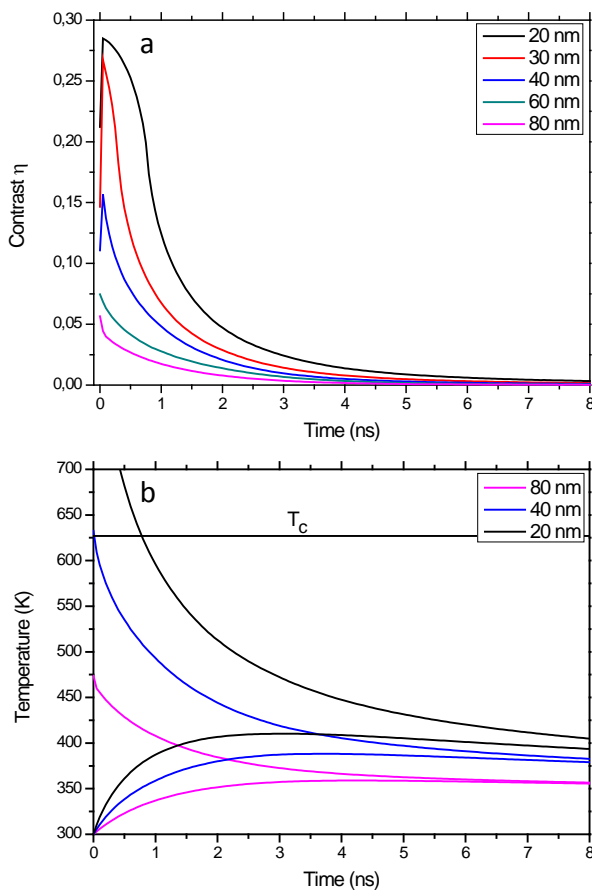


**Figure 4.9:** Thickness dependence. Panel (a) shows contrast curves for various film thicknesses. The corresponding temperature dynamics are shown for three selected thicknesses in panel (b), each represented by two film temperature curves: the temperature at the 'hot' spot (downward curves) and 'cold' spot (upward curves starting from room temperature at  $t = 0$ ), averaged over the film thickness. Fluence  $F_0 = 5.0 \text{ mJ/cm}^2$ , grating wavelength  $\Lambda = 1.1 \mu\text{m}$ , SLG substrate.

Figure 4.9a,b shows the contrast curves and temperature dynamics for nickel film thicknesses varying from  $d = 20\text{ nm}$  to  $80\text{ nm}$ . The film thickness determines the amount of nickel in which the pump pulse energy is deposited. This affects the temperature after the initial equilibration across the film thickness. The energy per nickel volume unit is larger for thin films, resulting in a larger initial rise in temperature at the hot spots, see Figure 4.9b. The initial temperature increase is inversely proportional to film thickness. The hot spot is heated by  $\Delta T \approx 170\text{ K}$  for an  $80\text{ nm}$  film using a fluence of  $10\text{ mJ/cm}^2$ . Decreasing the thickness by a factor of two to  $40\text{ nm}$  doubles this to  $\Delta T \approx 340\text{ K}$ .

This film thickness dependence of maximum temperatures affects the contrast dynamics in a similar fashion as the fluence dependence: both a doubling of fluence as a halving of film thickness doubles the initial rise in temperature. The main difference is that a doubling in fluence doubles the energy, so that the diffusion into the substrate takes longer compared to the halving of the nickel film, so that, in the former, the attained contrast persists for longer time scales. This can be observed by comparing the wider ‘shoulder’ in the  $10\text{ mJ/cm}^2$  curve in Figure 4.8a to the thinner shoulder in the  $20\text{ nm}$  curve in Figure 4.9. The former accounts for a doubling in fluence as compared to the  $5\text{ mJ/cm}^2 - 40\text{ nm}$  case, whereas the latter accounts for a reduction in thickness by a factor of 2.

### Grating Wavelength Dependence

The grating wavelength  $\Lambda$  determines the distance between the hot and cold regions. The smaller the wavelength, the faster lateral temperature equilibration occurs. Figure 4.10b shows that the minimum and maximum temperature approach each other faster for smaller  $\Lambda$ , despite equal temperatures at  $t = 0$  for all wavelengths. The temperature gap largely determines the contrast  $\eta$ , and therefore the contrast persists for longer for larger  $\Lambda$ . Comparing Figures 4.9 and 4.10 it can be observed that film thickness mostly impacts early contrast dynamics, whereas grating wavelength impacts later contrast dynamics.

### Substrate Dependence: SLG versus MgO

Lastly, a comparison is made between MgO and SLG as substrate materials. Table 4.1 shows that MgO has a significantly larger thermal conductivity than SLG (over 50 times larger). However, it was also shown in Section 4.3 that the interface between MgO and nickel has a nonzero Kapitza resistance. It can be seen in Figure 4.11 that cooling of the nickel film occurs

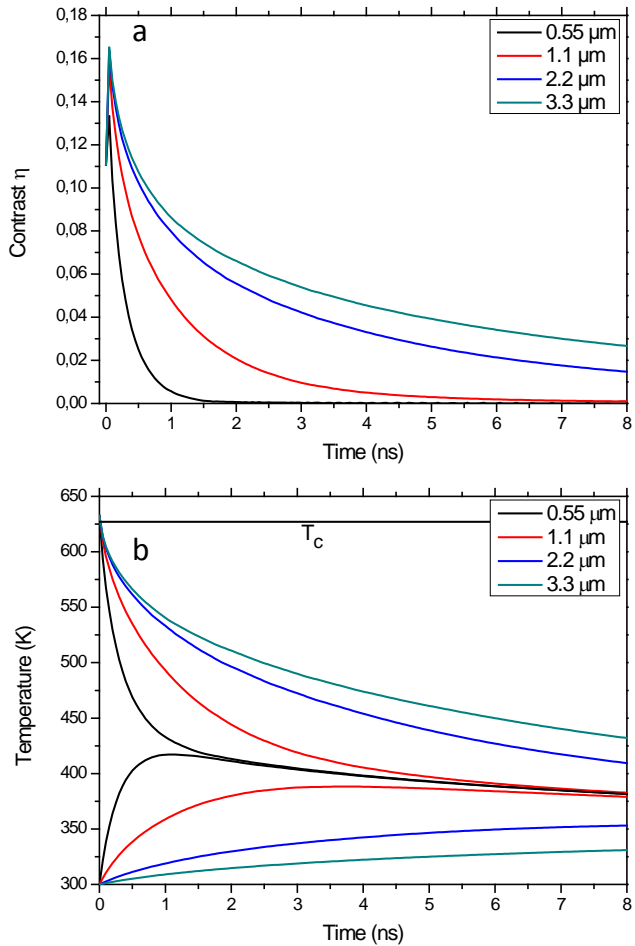


**Figure 4.10:** Grating wavelength dependence. Panel (a) shows contrast curves for grating wavelengths  $\Lambda$  varying from 0.55 to 3.3  $\mu\text{m}$ . The corresponding temperature dynamics are shown for three selected thicknesses in panel (b), each represented by two film temperature curves: the temperature at the ‘hot’ spot (downward curves) and ‘cold’ spot (upward curves starting at room temperature at  $t = 0$ ), averaged over the film thickness. For small values of  $\Lambda$ , the temperature gap closes quickly due to fast lateral equilibration, resulting in quickly reducing contrast curves. Fluence  $F_0 = 5.0 \text{ mJ/cm}^2$ , film thickness  $d = 40 \text{ nm}$ , SLG substrate.

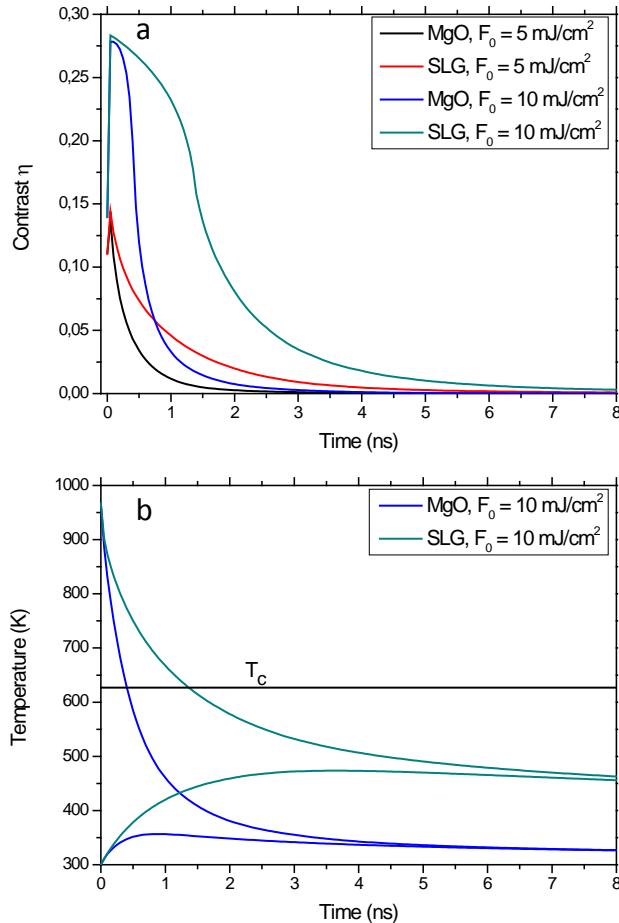


**Figure 4.11:** Substrate dependence. Panel (a) shows contrast curves for two substrates, SLG and MgO, at two different fluences. The corresponding temperature dynamics are shown for one of the fluences in panel (b), each case represented by two film temperature curves: the temperature at the 'hot' spot (downward curves) and 'cold' spot (starting at room temperature at  $t = 0$ ), averaged over the film thickness. The larger heat conductivity of MgO results in faster cooling of the nickel film despite the nonzero thermal boundary resistance, resulting in quicker magnetization and contrast dynamics. Fluence  $F_0 = 5.0 \text{ mJ/cm}^2$ , film thickness  $d = 40 \text{ nm}$ , grating wavelength  $\Lambda = 1.1 \mu\text{m}$ . Thermal boundary resistance for MgO curves:  $3.0 \cdot 10^{-9} \text{ K}\cdot\text{m}^2 / \text{W}$ .

much quicker using MgO substrates than SLG substrates. It can therefore be concluded that for MgO the difference in thermal conductivity has a stronger effect than the boundary resistance in terms of the heat flux from the nickel film to the substrate.

The faster cooling of the nickel film for MgO results in quicker contrast dynamics. The hot regions remagnetize faster, and therefore the contrast reduces faster for MgO than for SLG substrates. Magnetization precession will therefore be visible for longer time scales using SLG. Experimentally, SLG is therefore in most cases a better substrate material than MgO in the transient grating setup in terms of Faraday measurement sensitivity.

#### 4.6.3 Correction of Experimental Fluence Dependences

Knowing how the shape of the contrast curves changes as a function of fluence, grating wavelengths and film thickness allows us to quickly uncover the magnetization dynamics of complete experimental data sets. Figure 4.12 shows three fluence dependences before (left-hand subfigures) and after (right-hand subfigures) correction, at two different gratings wavelengths  $\Lambda$ . The data sets remain in the low-fluence regime throughout, meaning that the contrast curves do not show ‘bumps’, and complete demagnetization does not occur.

In the raw (background-subtracted) experimental data, precession amplitudes increase when the fluence increases (leaving other parameters constant). For corrected data, this is not necessarily the case. Subfigures (a) and (c) show fluence dependences at  $\Lambda = 1.1 \mu m$  where the magnetic field is tuned to SAW and SSLW resonance respectively. The corrected counterparts - subfigures (b) and (d) - reveal that at these experimental conditions, the amplitude of the magnetic wave is actually fluence-independent in this fluence regime. This could imply that the amplitude of the magnetic wave is saturated already at very low fluence values. For  $\Lambda = 1.3 \mu m$  (at SSLW resonance, subfigure (e)), the picture is more complex. Even though the experimental data shows a dramatic increase in amplitude when the fluence is increased, the corrected curves show that the amplitude actually goes down after an initial increase, with a maximum amplitude at approximately  $0.6 mJ/cm^2$ . This result shows that the fluence dependence of the magnetic wave amplitude does not behave in the same way for every grating wavelength, as well as that the amplitude is grating-dependent.

From the uncorrected data it is already evident that the SAWs have longer lifetimes than SSLWs, as expected (see Section 3.1.1). This becomes even more apparent after correction of the magnetic waves. Whereas the

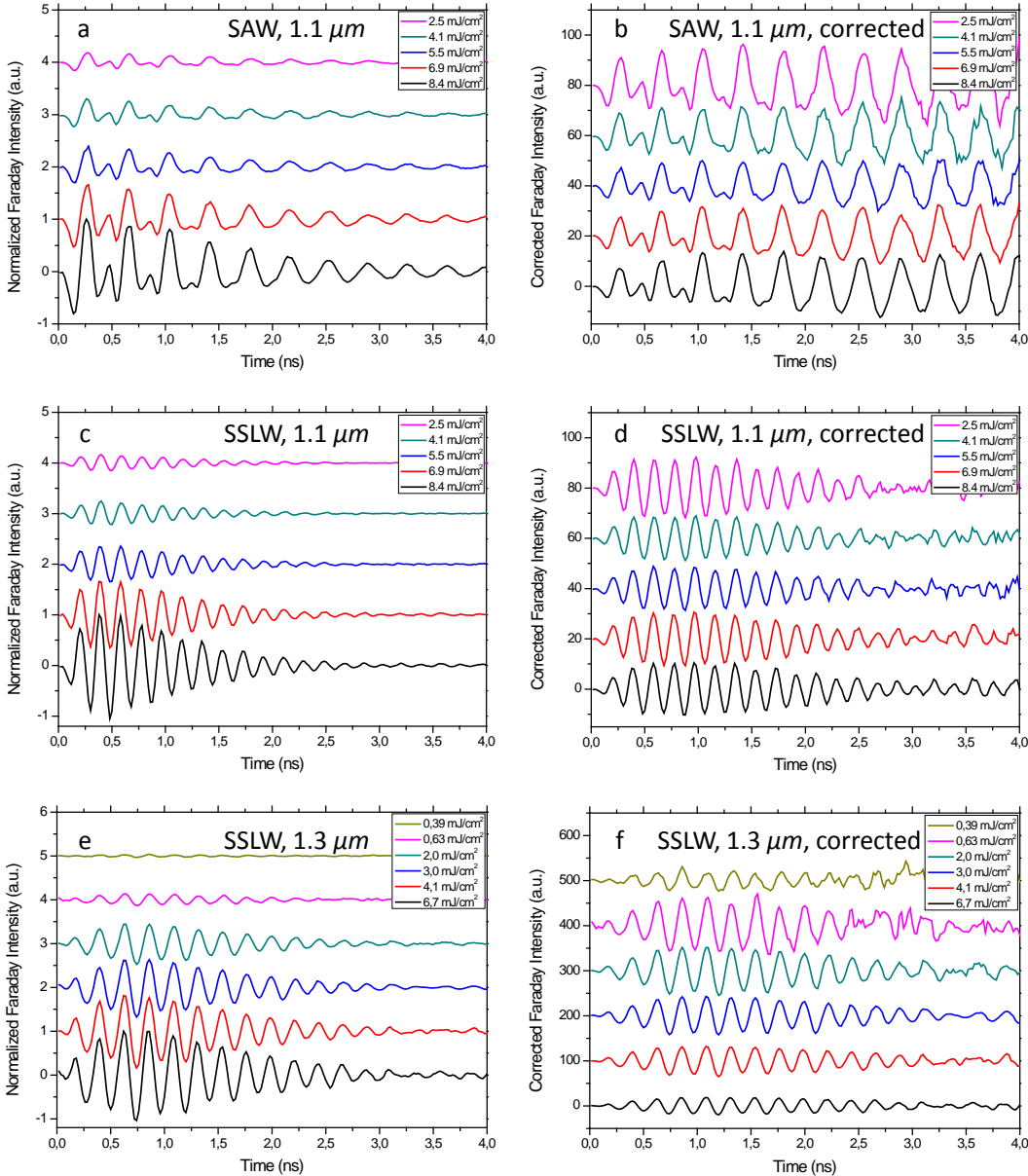


**Figure 4.12:** Experimental data before (left-hand subfigures) and after (right-hand subfigures) correction using contrast curves. Data consists of fluence dependences on a nickel sample of thickness  $d = 60\text{ nm}$ , using grating wavelengths  $\Lambda = 1.1\text{ }\mu\text{m}$  and  $1.3\text{ }\mu\text{m}$  at both SAW- and SSLW-resonant fields.

resonance due to the SSLWs begins to decrease in amplitude after  $1.5\text{ ns}$ , the SAW-induced resonances are observed to increase throughout the  $4\text{ ns}$  time window.

## 4.7 Conclusion and Outlook

The temperature simulations provide a tool to estimate time-resolved magnetic sensitivity during Faraday rotation measurements in the transient grating setup. The contrast curves can be used to evaluate and correct time traces, and enable the experimenter to select the appropriate grating wavelength, fluence, film thickness, and substrate material in order to optimize signal amplitudes for performing measurements. The method of obtaining the contrast curves involves some assumptions, making it difficult to determine their accuracy. For this reason, the author recommends performing Faraday rotation measurements at both SAW and SSLW resonant applied fields using different values for grating wavelength and fluence, and using multiple samples with varying film thicknesses and substrate materials. The accuracy of the contrast curves can then be evaluated by correcting time traces using the appropriate  $\eta$ -curves. The resulting corrected curves should show consistent behavior for both the long-living SAW and the highly damped SSLW oscillation amplitudes across the entire dataset. The methods of time-trace correction has lead to an estimation of the precessional angle of  $\approx 17^\circ$ . To test its accuracy the author recommends that the angle is determined via a different route as well. Possible techniques suitable to this end include device fabrication and subsequent inverse spin Hall effect measurements, and theoretical magnetoelastic calculations/simulations.

Chapter **5**

# Magnetoelastic Dynamics in Strongly Magnetostrictive Terfenol

## 5.1 Introduction

Previous chapters of this thesis emphasized spectroscopy on nickel. This chapter reports on the initial data acquired on Terfenol in the transient grating setup. Terfenol is a ferromagnetic material with structural formula  $TbFe_2$ . It is a special case of  $Tb_xDy_{1-x}Fe_2$ , or ‘Terfenol-D’, a class of materials developed and designed by the Naval Ordnance Laboratory (NOL) in the 70s [40] (The name Terfenol-D is an acronym of *Terbium*, *iron* (*Fe*), ‘*NOL*’, and *Dysprosium*). Terfenol shows the largest magnetostriction at room temperature of any material, with magnetostrictive coefficients (strain values) reported of  $\lambda = 2450 \text{ ppm}$  (along the [111]-direction) [41]. This makes Terfenol an interesting material to study in the TG setup. This chapter reports on the results of this study, although it is emphasized that the measurements and interpretation of the results are still in progress.

## 5.2 Results

The studied sample was created and provided by A. Hillion, V. Polewczyk, S. Andrieu, G. Malinowski, and K. Dumesnil from the Institut Jean Lamour of Université de Lorraine, and M. Anane from Unité Mixte de Physique CNRS/Thales, and consists of the following four layers: 1) a sapphire substrate with crystallographic orientation (11 – 20), 2) a 50 nm *Nb* buffer layer, 3) a 50 nm Terfenol ( $TbFe_2$ ) layer with crystallographic orienta-

tion (110), 4) a 250 nm  $SiO_2$  (silica) capping layer. The direction of the crystallographic vectors in the sample are yet unknown for all three crystalline layers of the sample. The creators of the sample have reported an out-of-plane magnetization component as well as in-plane magnetization isotropy, with corresponding coercive fields close to 1 T, exceeding the capabilities of the magnet employed in our experimental setup. Measurements were performed in the transient grating setup as depicted in Figure 2.3. Both the transmission TG diffraction signal as the Faraday rotation signal show anomalous behavior.

### 5.2.1 Faraday Rotation

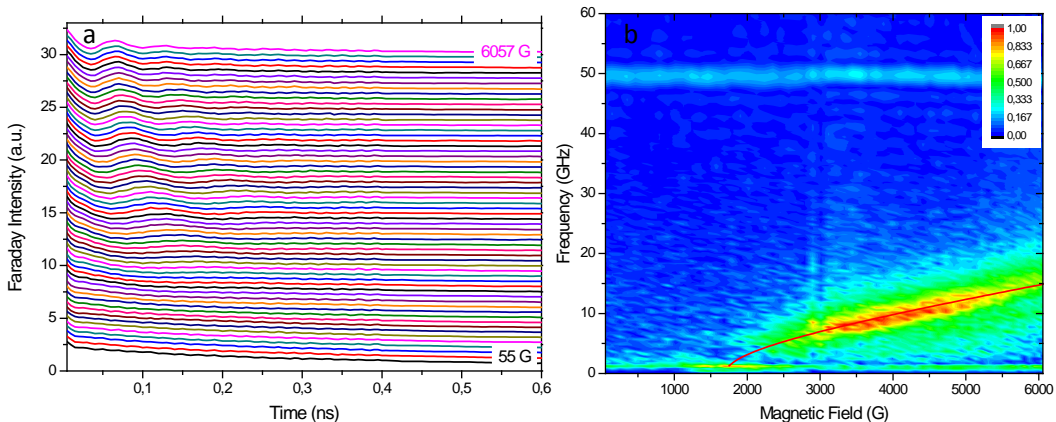


**Figure 5.1:** Faraday intensity for Terfenol. Panel (a) shows time traces as a function of applied in-plane magnetic field. Although the time axis extends only to 0.6 ns for visibility, data was taken up to 2.5 ns. The field goes from 55 G (remnant magnetization of the magnet) to 6057 G in steps of  $\approx 100$  G. Panel (b) shows the corresponding FFT spectra after background subtraction, along with the FMR curve in red.  $\Lambda = 2.9 \mu m$ .

Figure 5.1 shows the Faraday rotation response of Terfenol as a function of magnetic field strength. There are a few key differences compared to the (noncrystalline) nickel samples that were discussed in the previous chapters; see Figure 3.4 for the analogous FFT spectrum of a 40 nm nickel on SLG sample. Nickel shows FMR oscillations that can be fitted well using equation 3.3. The Terfenol sample shows FMR oscillations as well, however, the FMR curve does not intersect with the origin but rather at a finite magnetic field of  $\approx 1700$  G, signaling a high level of magnetic anisotropy. Whereas the nickel film shows FMR oscillations at large amplitudes only at the intersection with acoustic mode frequencies, the Ter-

fenol sample seems to have no such resonance events but rather gradually increases and decreases in amplitude, with a maximum amplitude occurring at around  $\approx 4000$  G. The field of 6057 G was the maximum attainable field strength for the magnet, and so the (FMR) behavior at field beyond this value is uncertain. Similar FMR behavior is also observed using a single pump excitation rather than the grating excitation, which shows that the FMR is grating-independent.

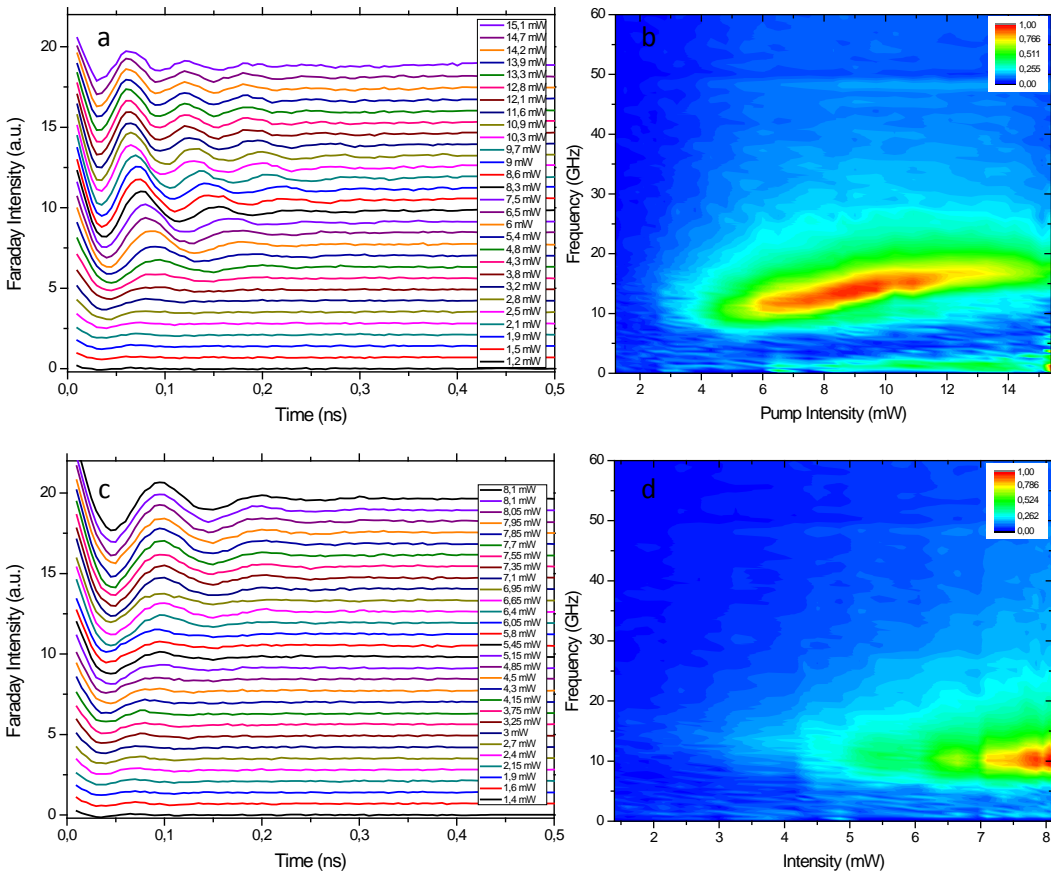


**Figure 5.2:** Faraday rotation amplitude for Terfenol as a function of pump intensity for both TG excitation (top panels) and single pump pulse excitation (bottom panels). Panel (a) and (c) show background-subtracted time traces as a function of pump intensity. Although the time axis extends only to 0.5 ns for visibility, data was taken up to 2.5 ns. Panels (b) and (d) show the corresponding FFT spectra. Applied field  $H = 6057$  G,  $\Lambda = 2.0 \mu\text{m}$  for the double-pump (TG) scan.

Two field-independent frequency ‘bands’ can be observed in the FFT spectrum as well. At the lower end of the frequency spectrum a band is present at around  $\approx 1$  GHz. A second band is present at  $\approx 50$  GHz. The

latter appears broadened due to undersampling in the time domain for  $t > 0.4 \text{ ns}$  in order to reduce the measurement time. The origin of both the high and low frequency response is uncertain, although their field-independent behavior possibly reflects acoustic degrees of freedom rather than dynamics in the magnetization of the sample. The lower band does not seem to correspond to the SAW seen in the TG diffraction channel, which is observed at a slightly higher frequency.

A dependence of the Faraday response to the pump intensity was also performed, both for TG excitation as well as for single pump excitation. In Figure 5.2, it can be seen that increasing TG pump power not only results in larger Faraday amplitudes, but also results in an increase in FMR frequency. For single pump excitation, the FMR frequency seems to remain constant when the fluence is varied, although the frequency trend is not known above 8 mW (the maximum single pump excitation power).

### 5.2.2 Transmission TG Diffraction

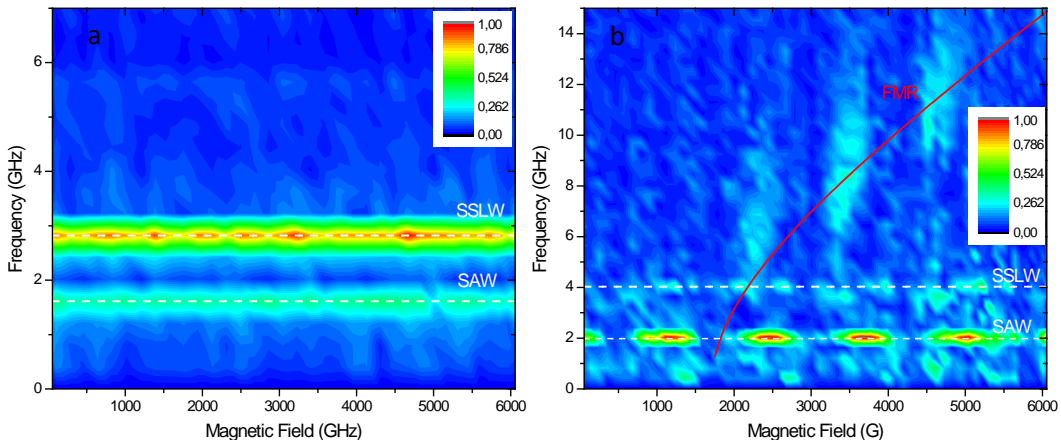


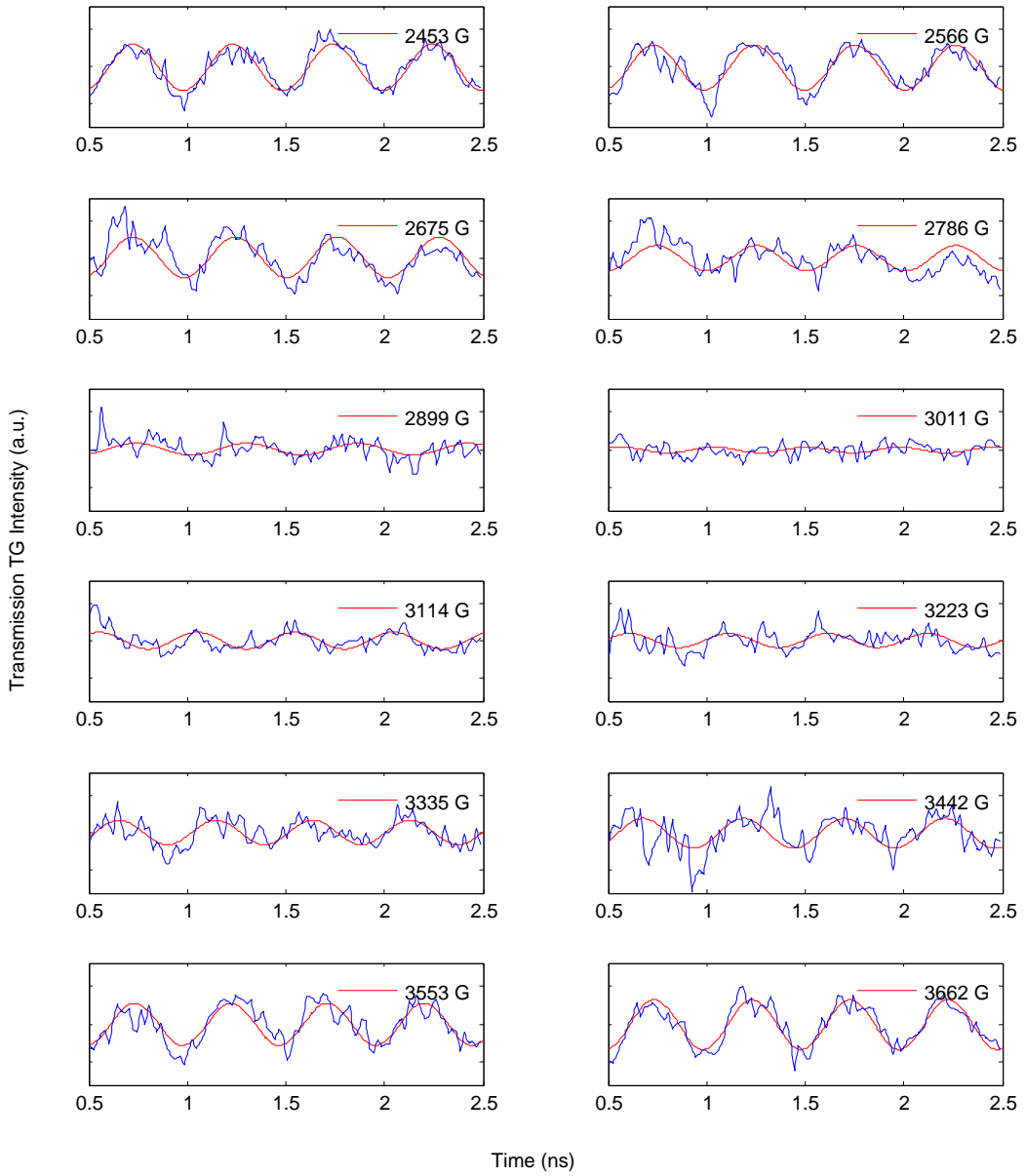
**Figure 5.3:** Frequency spectra of transmission TG diffraction intensity for (a) nickel and (b) Terfenol, after background subtraction. Grating wavelength  $\Lambda = 2.0 \mu\text{m}$  for nickel and  $\Lambda = 2.9 \mu\text{m}$  for Terfenol. SAW and SSLW acoustic modes are shown as white dashed lines. The FMR curve for Terfenol is shown as the red solid line, and is identical to the curve in Figure 5.1b. The TG diffraction signal for nickel is not dependent on applied magnetic field. For Terfenol the spectrum shows many field-dependent features such as the presence of FMR frequencies and beating in the acoustic modes.

The acoustic waves are field-independent for nickel, and so TG diffraction time traces and their Fourier Transforms are identical at every field,

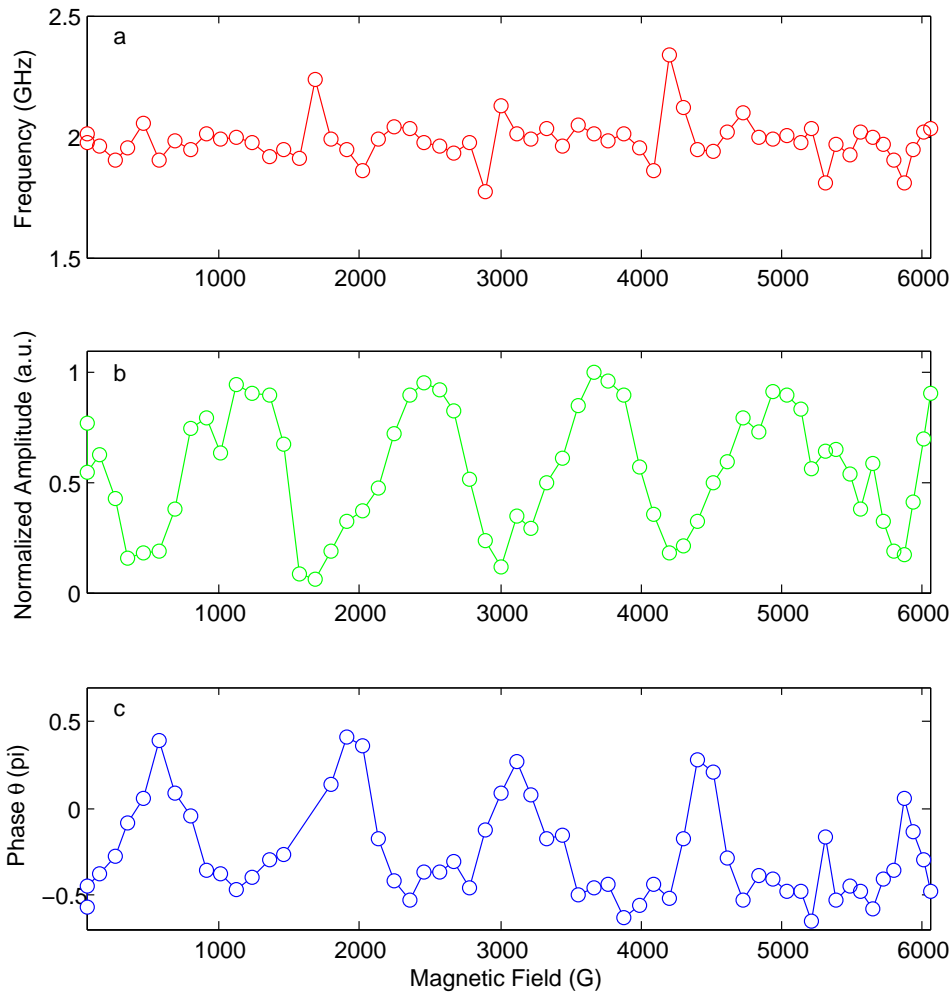
as can be seen in Figure 5.3a. Our study on Terfenol reveals acoustic sensitivity to the applied field, in stark contrast to the nickel samples. Figure 5.3b shows Fourier Transforms of transmission TG diffraction time traces as a function of magnetic field. The first deviation from the ‘usual’ spectra seen in nickel, is the feature that the intensity due to diffraction from the SAW and SSLW acoustic modes oscillates as a function of field. The reproducible pattern is very periodic and has a oscillation period of approximately 1300 G. The relative SSLW amplitude as compared to the SAW amplitude depends on the orientation of the sample during the experiments. The phase of the beating pattern in the TG arm is not constant over multiple data sets; even zero-field time traces do not consistently show either oscillations or absence of oscillations. The beating in the fingerprint of the acoustic waves is significant as it implies that the magnetic state of the sample couples back to the acoustic modes. The beating pattern is unexplained as of yet, but possibilities include interference between acoustic and magnetic waves, and strain-induced quenching of the acoustic waves due to the large magnetoelasticity.

Figure 5.4 shows a subset of the transmission TG diffraction time traces. The curves are fitted using a simple sine wave function to extract the frequency, amplitude, and phase as a function of applied field. These fitting components are plotted in Figure 5.5 for the entire data set. The frequency remains approximately constant and corresponds to the SAW frequency. The largest deviations correspond to small amplitudes, reducing the reliability of these fits. The amplitude oscillates in field, reflecting the beating pattern that was already visible in the FFT spectrum (Figure 5.3b). The phase, a quantity not visible in the FFT plot, also shows oscillations with a similar period as the amplitude. The phase oscillates roughly between  $-\pi/2$  and  $+\pi/2$ , implying a  $180^\circ$  phase flip. A phase of  $-\pi/2$  seems to be corresponding to large acoustic wave amplitudes, a phase of  $+\pi/2$  seems to suppress the acoustic wave. This may signal constructive and destructive interference between the (Rayleigh) acoustic wave and another (magnetic or elastic) wave mode, but the cause of the phase shift and how this leads to modulation in the amplitudes is unclear.

A second important departure from our previous measurements on nickel is the emergence of FMR frequencies in the diffraction channel. It was previously thought that the magnetic wave only impacts the Faraday rotation and is therefore only visible in our setup during Faraday detection measurements; FMR frequencies have never been seen during TG diffraction measurements in nickel. Their presence for Terfenol implies that the magnetic state (*i.e.* the phase in the FMR oscillations) causes structural deformation and changes the diffraction efficiency, or that the precessional



**Figure 5.4:** Transmission TG diffraction time traces (blue curves) at applied magnetic field values between 2453 G and 3662 G (values shown in upper-right corner of each subplot). The curves are fitted with a sine wave (red curves) to extract phase, frequency and amplitude information. Data at times  $t < 0.5$  ns are not incorporated in order to avoid the FMR oscillations, which are sufficiently damped after this time.



**Figure 5.5:** Result of the fitting parameters of the transmission TG diffraction time traces, of which a subset is shown in Figure 5.4. a) Frequency. b) Amplitude (normalized). c) Phase, in units of  $\pi$ . The frequency appears to remain constant in field, whereas the amplitude and the phase show oscillatory behavior.

phase of the spin wave leads to changes in the refractive index significantly enough to lead to diffraction. The FMR frequencies show similar beating behavior as the SAW and SSLW modes. The beating period is the same but the phase is different, with the FMR beating preceding the acoustic modes in field by roughly  $\pi/2$ .

Recent measurements on a 300 nm Terfenol sample without additional overlayer still show beating of the acoustic mode during reflection TG diffraction measurements (the sample is too optically dense for transmission TG). As reflection TG diffraction only shows intensity due to diffraction from the modulation depth (elastic/acoustic wave) due to the grating, the presence of the beating pattern in this type of detection indicates that it is in fact the elastic wave that is quenched periodically in field. The results also remove the possibility that the features of the other sample are due to the presence of the 250 nm  $SiO_2$  overlayer.

### 5.3 Conclusion and Outlook

Terfenol shows several interesting features that, to the best of the author's knowledge, have not been observed before. The TG diffraction channel, known to measure acoustic wave propagation, shows a pronounced beating pattern as a function of magnetic field, both for the precession amplitude as well as for the phase. Additionally, the channel not only shows the traditional acoustic waves modes, but FMR oscillations are visible as well. Observing the magnetic behavior through the Faraday detection scheme also reveals the same FMR curve, as expected. The shape of this curve is however different from the case of nickel in that the intersection with the acoustic modes (SAW and SSLW) does not amplify the intensity, and that the curve does not intersect the origin.

The data point towards strong interaction between elastic and magnetic degrees of freedom, and demonstrate the potential for magnetic control over structural deformations. Numerical simulations should be employed in order to gain a more thorough understanding of acoustic wave propagation in highly magnetostrictive thin films on a dielectric substrate and their coupling to the magnetic degrees of freedom. A clear knowledge of the direction of the crystallographic axes for both the sapphire substrate, the niobium buffer layer and the Terfenol film may prove useful in the interpretation of the anomalous effects as well.

# Conclusion

An all-optical route is applied to study magnetoelastic coupling in ferromagnetic thin films. The transient grating setup, which is based on the pump-probe philosophy, is implemented in order to launch frequency tunable surface acoustic waves due to the periodic excitation pattern from two interfering pump pulses. By incorporating both a TG diffraction detector as well as a Faraday Rotation detection scheme, this setup allows us to simultaneously follow the elastic waves as well as their coupling to the magnetic degrees of freedom with sub-picosecond resolution.

The main results of this thesis fall in two broad categories. Firstly, a method is provided to calculate the time-dependent sensitivity to magnetization dynamics in the transient grating setup. This is a non-trivial process, as magnetization amplitude relies on temperature distributions inside the magnetic thin film. To this end, finite element methods are employed in order to simulate the temperature dynamics in our samples consisting of both a thin film as well as a substrate. Subsequent calculations of the corresponding changes in (de)magnetization allows us to reconstruct the magnetization vector from experimental data as a function of time. This is important because it enables accurate estimations of various characteristics of both the magnetic and elastic waves, such as amplitudes, precession angles and damping constants.

Secondly, initial experimental results are reported on the strongly magnetostrictive material Terfenol in the transient grating setup. The results are unusual for multiple reasons. In the Faraday channel FMR oscillations are present, but, contrary to previous findings for nickel samples, the FMR does not resonantly couple to any acoustic mode. The frequency of the FMR changes with pump intensity, however the data seem to suggest that this occurs only when a grating is applied. In the TG diffraction

channel, it is found that acoustic modes seem to be suppressed at regular intervals when the applied magnetic field strength is varied. To the best of the author's knowledge, this is unprecedented, and is in strong contrast to the case of nickel, for which the diffraction channel does not show any field-dependent behavior. Moreover, the diffraction channel is sensitive to the same frequencies that are observed in the Faraday channel, which also show the beating pattern at equal intervals as the acoustic modes, but different phase. Understanding of these phenomena is still limited, calling for both additional experimental as well as theoretical work.

## Acknowledgements

This research would not have been possible without the help and support of many people. Firstly, I would like to thank Ron Tobey for providing the opportunity to perform my master's research project in his group. Thank you, Ron, for taking the time to teach how to efficiently conduct an experiment, and for your guidance during the project and during the process of writing the thesis. Secondly, I would like to thank my two daily supervisors, Julius Janušonis and Chia-Lin Chang. The discussions with Julius and the lab-sessions with Chia-Lin were really helpful and essential to my project. Qi Liu, thank you for help in the lab on the Terfenol project, and building the TG setup together with Joop Hendriks. I would also like to thank Foppe de Haan for providing assistance in using computer software and lab equipment. Mart Salverda, thank you for conducting XRD analysis on several of the samples that I used. Viktor Shalagatskyi, I would like to thank you for providing your simulation files, which quickly got me up to speed on the temperature analyses. I would also like to thank A. Hillion, V. Polewczyk, S. Andrieu, G. Malinowski, K. Dumesnil, and M. Anane for making their Terfenol samples available for use in our setup. Lastly, I would like to thank the entire Optical Condensed Matter Physics (OCMP) group for providing a nice atmosphere and making the entire period enjoyable. I enjoyed working with all of you. The project required many different skill sets, and, as a result, I have learned a lot along the way.



# Bibliography

- [1] L. Martin, S. Crane, Y. Chu, M. Holcomb, M. Gajek, M. Huijben, C. Yang, N. Balke, and R. Ramesh, *Multiferroics and magnetoelectrics: thin films and nanostructures*, Journal of Physics: Condensed Matter **20**, 434220 (2008).
- [2] B. B. Van Aken, T. T. Palstra, A. Filippetti, and N. A. Spaldin, *The origin of ferroelectricity in magnetoelectric YMnO<sub>3</sub>*, Nature materials **3**, 164 (2004).
- [3] R. Ramesh and N. A. Spaldin, *Multiferroics: progress and prospects in thin films*, Nature materials **6**, 21 (2007).
- [4] T. Kimura, T. Goto, H. Shintani, K. Ishizaka, T. Arima, and Y. Tokura, *Magnetic control of ferroelectric polarization*, nature **426**, 55 (2003).
- [5] N. A. Hill, *Why are there so few magnetic ferroelectrics?*, The Journal of Physical Chemistry B **104**, 6694 (2000).
- [6] S. Tehrani et al., *Magnetoresistive random access memory using magnetic tunnel junctions*, Proceedings of the IEEE **91**, 703 (2003).
- [7] T. Devolder and C. Chappert, *Cell writing selection when using precessional switching in a magnetic random access memory*, Journal of applied physics **95**, 1933 (2004).
- [8] L. Thevenard, I. S. Camara, S. Majrab, M. Bernard, P. Rovillain, A. Lemaître, C. Gourdon, and J.-Y. Duquesne, *Precessional magnetization switching by a surface acoustic wave*, Physical Review B **93**, 134430 (2016).

- [9] G. Maugin and A. Hakmi, *Magnetoelastic surface waves in elastic ferromagnets—I: Orthogonal setting of the bias field*, The Journal of the Acoustical Society of America **77**, 1010 (1985).
  - [10] R. Camley, *Magnetoelastic waves in a ferromagnetic film on a nonmagnetic substrate*, Journal of Applied Physics **50**, 5272 (1979).
  - [11] K.-i. Uchida, T. An, Y. Kajiwara, M. Toda, and E. Saitoh, *Surface-acoustic-wave-driven spin pumping in  $Y_3Fe_5O_{12}/Pt$  hybrid structure*, Applied Physics Letters **99**, 212501 (2011).
  - [12] L. Dreher, M. Weiler, M. Pernpeintner, H. Huebl, R. Gross, M. Brandt, and S. Goennenwein, *Surface acoustic wave driven ferromagnetic resonance in nickel thin films: Theory and experiment*, Physical Review B **86**, 134415 (2012).
  - [13] M. Weiler, H. Huebl, F. Goerg, F. Czeschka, R. Gross, and S. Goennenwein, *Spin pumping with coherent elastic waves*, Physical review letters **108**, 176601 (2012).
  - [14] A. Scherbakov, A. Salasyuk, A. Akimov, X. Liu, M. Bombeck, C. Brüggemann, D. Yakovlev, V. Sapega, J. Furdyna, and M. Bayer, *Coherent magnetization precession in ferromagnetic (Ga, Mn)As induced by picosecond acoustic pulses*, Physical review letters **105**, 117204 (2010).
  - [15] J.-W. Kim, M. Vomir, and J.-Y. Bigot, *Ultrafast magnetoacoustics in nickel films*, Physical review letters **109**, 166601 (2012).
  - [16] J. Janušonis, C. Chang, P. van Loosdrecht, and R. Tobey, *Frequency tunable surface magneto elastic waves*, Applied Physics Letters **106**, 181601 (2015).
  - [17] J. A. Rogers, A. A. Maznev, M. J. Banet, and K. A. Nelson, *Optical generation and characterization of acoustic waves in thin films: Fundamentals and applications*, Annual Review of Materials Science **30**, 117 (2000).
  - [18] T. F. Crimmins, A. Maznev, and K. A. Nelson, *Transient grating measurements of picosecond acoustic pulses in metal films*, Applied physics letters **74**, 1344 (1999).
  - [19] A. N. Cleland, *Foundations of nanomechanics: from solid-state theory to device applications*, Springer Science & Business Media, 2013.
-

- [20] J. Janušonis, C. Chang, T. Jansma, A. Gatilova, A. Lomonosov, V. Shalagatskyi, V. Vlasov, V. Temnov, and R. Tobey, *Ultrafast Magnetoelastic Probing of Surface Acoustic Transients*, arXiv preprint arXiv:1601.04350 (2016).
  - [21] Q. Shen, A. Harata, and T. Sawada, *Theory of transient reflecting grating in fluid/metallic thin film/substrate systems for thin film characterization and electrochemical investigation*, Japanese journal of applied physics **35**, 2339 (1996).
  - [22] A. R. Duggal, J. A. Rogers, and K. A. Nelson, *Real-time optical characterization of surface acoustic modes of polyimide thin-film coatings*, Journal of applied physics **72**, 2823 (1992).
  - [23] M. Weiler, L. Dreher, C. Heeg, H. Huebl, R. Gross, M. Brandt, and S. Goennenwein, *Elastically driven ferromagnetic resonance in nickel thin films*, Physical review letters **106**, 117601 (2011).
  - [24] M. Faraday, *On the magnetization of light and the illumination of magnetic lines of force*, Royal Society, 1846.
  - [25] M. Kaganov, I. Lifshitz, and L. Tanatarov, *Relaxation between electrons and the crystalline lattice*, Soviet Physics Jetp-Ussr **4**, 173 (1957).
  - [26] S. Anisimov, B. Kapeliovich, and T. Perelman, *Electron emission from metal surfaces exposed to ultrashort laser pulses*, Zh. Eksp. Teor. Fiz. **66**, 375 (1974).
  - [27] P. Kapitza, *The study of heat transfer in helium II*, J. Phys.(USSR) **4**, 181 (1941).
  - [28] C. Kittel, *Introduction to solid state physics*, Wiley, 2005.
  - [29] J. Janušonis, T. Jansma, C. Chang, Q. Liu, A. Gatilova, A. Lomonosov, V. Temnov, and R. Tobey, *Transient Grating Spectroscopy in Magnetic Thin Films: Simultaneous Detection of Elastic and Magnetic Dynamics*, Scientific Reports **6**, 29143 (2016).
  - [30] V. Shalagatskyi, *Ultrafast acoustics in hybrid and magnetic structures*, (2015).
  - [31] Z. Lin, L. V. Zhigilei, and V. Celli, *Electron-phonon coupling and electron heat capacity of metals under conditions of strong electron-phonon nonequilibrium*, Physical Review B **77**, 075133 (2008).
-

- [32] R. Wheast, *Handbook of chemistry and physics*, CRC press, 1976.
- [33] N. Bansal and R. Doremus, *Handbook of glass properties*. 1986.
- [34] A. M. Hofmeister, *Thermal diffusivity and thermal conductivity of single-crystal MgO and Al<sub>2</sub>O<sub>3</sub> and related compounds as a function of temperature*, Physics and Chemistry of Minerals **41**, 361 (2014).
- [35] A. D. Rakić, A. B. Djurišić, J. M. Elazar, and M. L. Majewski, *Optical properties of metallic films for vertical-cavity optoelectronic devices*, Applied optics **37**, 5271 (1998).
- [36] <http://ocmp.phys.rug.nl/Timen/1.gif>. Fluence  $F = 10 \text{ mJ/cm}^2$ , film thickness  $d = 40 \text{ nm}$ , grating wavelength  $\Lambda = 1.1 \mu\text{m}$ .
- [37] <http://ocmp.phys.rug.nl/Timen/2.gif>. Fluence  $F = 19.5 \text{ mJ/cm}^2$ , film thickness  $d = 40 \text{ nm}$ , grating wavelength  $\Lambda = 1.1 \mu\text{m}$ .
- [38] I. S. Grigoriev and Meř, *Handbook of physical quantities*.
- [39] L. Thevenard, J.-Y. Duquesne, E. Peronne, H. J. Von Bardeleben, H. Jaffres, S. Ruttala, J. George, A. Lemaître, and C. Gourdon, *Irreversible magnetization switching using surface acoustic waves*, Physical Review B **87**, 144402 (2013).
- [40] M. B. Moffett, A. E. Clark, M. Wun-Fogle, J. Linberg, J. P. Teter, and E. A. McLaughlin, *Characterization of Terfenol-D for magnetostrictive transducers*, The Journal of the Acoustical Society of America **89**, 1448 (1991).
- [41] A. Clark and D. Crowder, *High temperature magnetostriction of TbFe<sub>2</sub> and Tb<sub>27</sub>Dy<sub>73</sub>Fe<sub>2</sub>*, IEEE transactions on magnetics **21**, 1945 (1985).